Cement and Concrete Research 153 (2022) 106697

Contents lists available at ScienceDirect

Cement and Concrete Research

journal homepage: www.elsevier.com/locate/cemconres

# In-situ formation of layered double hydroxides (LDHs) in sodium aluminate activated slag: The role of Al-O tetrahedra

Tao Liu [a,b], Qingliang Yu [a,b,*], H.J.H. Brouwers [b,c]

[a] School of Civil Engineering, Wuhan University, Wuhan 430072, PR China
[b] Department of the Built Environment, Eindhoven University of Technology, 5600MB, Eindhoven, the Netherlands
[c] State Key Laboratory of Silicate Materials for Architectures, Wuhan University of Technology, Wuhan 430070, PR China

ARTICLE INFO

*Keywords:*
$NaAlO_2$ activated slag
In-situ formed LDH
Pore solution
Pore structure
Chloride absorption

ABSTRACT

Alkali activated materials (AAMs) have gained great attention as a new low-carbon binder. However, their durability performance, e.g. chloride ingress resistance, still needs further improvement. This study attempts to enhance the chloride binding of AAMs by activating slag with sodium aluminate with the aim to promote the in-situ formation of layered double hydroxides (LDHs). The evolution of pH and ions in the pore solution, reaction products and microstructure were determined to investigate the dynamic activation process. Results show that the sodium aluminate stabilizes the pH environment at around 12.7 during the curing ages. The Mg-Al-LDH with higher Al-O tetrahedra (denoted as $Al(OH)_4^-$) contents is promoted, enhancing the chloride absorption capacity. A new reaction mechanism is proposed to describe the activation process. This study reveals that the extra $Al(OH)_4^-$ in a relatively low pH environment prevents the competition between $Mg^{2+}$ and Si-O tetrahedra to react with $Al(OH)_4^-$, promoting the formation of LDH and C(N)-A-S-H simultaneously.

## 1. Introduction

Alkali activated materials (AAMs) have shown to be a promising alternative to Portland cement. However, its long-term performance, as well as the involved mechanisms under different exposure environments, are still not well understood. Many efforts have been spent on enhancing the chloride resistance of AAMs, but the effects are limited [1–3]. Besides, the high pH of AAMs also showed human toxicity which limits its practical application [4]. The effect of amorphous gels and the crystalline phases in the hardened cementitious materials are investigated pertaining to chloride resistance [5,6]. Layered double hydroxides (LDHs), one of the secondary reaction products of alkali activated ground granulated blast-furnace slag (GGBS), can absorb the anions, e.g. chloride ion, in the matrix [7]. The incorporation of ex-situ synthetic LDHs in the AAMs systems has been investigated and the LDHs showed high effectiveness in terms of chloride binding [8,9]. However, external-added LDHs absorb a large amount of water during the casting, which limits the total content of external LDHs in the AAMs matrix [10]. Besides, the costly and complicated synthesis process also highly limits the external LDHs application in the AAMs matrix to tackle the chloride ingress issue [9,11]. Moreover, promoting the in-situ formation of LDHs to replace the external-added LDHs AAM has not been well addressed.

Chloride ingress is one of the most prominent issues in AAMs. The chloride resistance is influenced by chemical binding through reaction products and physical absorption via pores and reaction products [3]. From the aspect of reaction products, the incorporation of ex-situ synthetic LDHs shows the virtuous performance of chloride resistance attributing to its physical absorption (major contribution) and chemical binding (minor contribution) of chloride ions [6,8,9]. Xu et al. [12] synthesized $Mg-Al-NO_3-LDH$ and $Mg-Al-NO_2-LDH$, finding that the chloride binding and corrosion resistance are increased by both LDHs additions. Qu et al. [10] reported that smaller particle size of $Mg-Al-NO_3-LDH$ improved the microstructure, meanwhile, the LDH material promoted the chemical chloride binding capacity of the matrix. Moreover, Ke et al. [13] examined the chloride removal by Mg-Al and Ca-Al LDHs in the simulated pore solution of alkali activated slag cement and found that the chloride binding was due to ion exchange and surface adsorption. At the same time, the chloride uptake was sensitive to pH change in the pore solution. Mundra et al. [14] simulated the chloride transport in AAMs and found that the Ca-Al LDH increased in the low MgO system while the Mg-Al LDH increased in the high MgO system. Both Ca-Al and Mg-Al LDH postpone the chloride ingress and increase chloride resistance. Besides, it is also worth mentioning that the Mg-Al LDH shows better chloride binding capacity than Ca-Al LDH. However

---

* Corresponding author at: School of Civil Engineering, Wuhan University, Wuhan 430072, PR China.
*E-mail address:* q.yu@bwk.tue.nl (Q. Yu).

https://doi.org/10.1016/j.cemconres.2021.106697
Received 7 June 2021; Received in revised form 7 December 2021; Accepted 18 December 2021

considering the water absorption of LDHs during casting, the content of LDHs in the AAMs system is usually lower than 4 wt% of binder as otherwise the large water demand would compromise other properties [9,10], which significantly limits the chloride binding capability of AAMs. Ye et al. [11] reported the autogenous formation and the behaviors of nitrite- and nitrate-intercalated LDHs in Portland cement-metakaolin-dolomite (OPC-MK-DM) blends. While the authors attempted to increase the autogenous formation of AFm (Ca-Al LDHs), they suggested that the incorporation of $NO_2^-$ and $NO_3^-$ harmed the evolution of microstructure despite the $NO_2^-$ and $NO_3^-$ anions preferably occupied the interlayer space of LDHs phases. Also, the increase of OPC replacement ratio from 30% to 45% in the ternary OPC-MK-DM systems lowered the degree of reaction and amount of reaction products. Therefore, the amount of LDHs phases was limited. Consequently, the autogenous formation of LDHs contributed little impact to the chloride binding capacity. These studies reveal that the chemical binding of chloride ions in AAMs is intensively affected by the amount of LDHs [9,15]. Thereby, the increase of in-situ formed LDHs in the AAMs could increase the chloride binding capacity. It is thus hypothesized that the increase of in-situ synthetic LDHs has a high potential for a remarkable increase in the chloride resistance of AAMs.

The skeleton of LDHs consists of two metal ions, one is a divalent cation (e.g. $Mg^{2+}$), and the other one is a trivalent cation (e.g. $Al^{3+}$) [16]. The concentration of aluminate (one type of normal trivalent metallic ions in LDH) in the pore solution of the AAMs matrix is one of the most important factors influencing the crystallization of the LDHs [17]. Meanwhile, the condition of Mg-Al LDH crystallization requires a relatively lower pH environment than the normal alkali activated solution, ranging from 9– 11 [16]. Thus, the sodium aluminate solution, in this research, is hypothetically introduced as an activator to control (1) the Al-O tetrahedra (hereafter denoted as $Al(OH)_4^-$) concentration and (2) a relatively low pH value in the pore solution of the AAM matrix to enhance the in-situ formed LDHs. Thereby, the comprehension of the mechanism of in-situ formed LDHs in AAMs is critical to understand how the sodium aluminate promotes the formation of LDHs. Moreover, the $Al(OH)_4^-$ participates in the process of gels formation. However, the mechanism of how the sodium aluminate affects the formation of calcium (sodium) aluminosilicate hydrates (C(N)-A-S-H) phases still remains poorly understood.

To discuss it further, the other physical aspects of chloride resistance, e.g. the lower porosity and more complex tortuosity of the microstructure in the AAMs matrix, in general, contribute to decreasing the chloride penetration. The complex distribution of pore diameter ranges and pore connections have a huge effect on ions' transport property [18]. Gel formation is the important factor influencing the evolution of microstructure, while the content of Si-O and Al-O tetrahedra, pH value, and other ions in the pore solution influence the gel formation. Under a given alkali content, the $SiO_2$ to $Na_2O$ molar ratio improves the microstructure evolution at the early stage [19], benefiting the transport parameters and enhancing the chloride resistance of AAMs [20]. Similarly, the $Al_2O_3$ to $Na_2O$ molar ratio also influences the gel formation, affecting the pore evolution [21]. The $Al_2O_3$ mainly comes from the solid precursors, while the proposed sodium aluminate activator providing a large amount of $Al(OH)_4^-$ could directly participate in the reaction [22]. The sodium aluminate activator was also investigated to generate more ettringite and calcium silicate hydrate (C-S-H), resulting in the strength increase [23]. The formation of more gels refines the microstructure, increasing the physical chloride binding ability. Therefore, the sodium aluminate is hypothetically an appropriate activator, as it can provide both (1) available Al-O tetrahedra and (2) a low pH environment for the LDH and gel formation, because the extra $Al(OH)_4^-$ could prevent competition between LDH and gel capturing $Al(OH)_4^-$ during the process of reaction. Whereas the mechanism of how the $Al(OH)_4^-$ in sodium aluminate activator promotes the formation of LDHs and gels remains unknown in terms of alkali activated slag, and specifically, the insufficient understanding about the ions changes of pore solution explaining the phases evolution and in-situ formed LDHs and gel.

This study investigates the mechanism of how the $Al(OH)_4^-$ influences in-situ synthetic LDH and gels formation in sodium aluminate activated slag (SAAS), and the consequent chloride absorption performance. The changes of pH value and ions in the pore solution of SAAS paste were tested to reveal the behavior of $Al(OH)_4^-$ in sodium aluminate that affects the Mg-Al LDH and gels formation at different curing ages. The reaction heat flow, reaction products as well as microstructure were determined to understand the activation process. A reaction mechanism was proposed to give an insight into the promotion of in-situ formed LDH and gels by sodium aluminate activator.

## 2. Experiment

### 2.1. Materials and sample preparations

Ground granulated blast-furnace slag (GGBS) was used in this study. The chemical compositions were determined by X-ray fluorescence (XRF), as shown in Table 1. The crystalline structure was determined by X-ray diffraction, as shown in Fig. 1. The particle size distribution (PSD) of the powder feedstocks was determined by laser granulometry, using a Master Sizer laser granulometry with an open measuring cell. The preparation of the powders was done by wet dispersion in deionized water. The particle size distribution is shown in Fig. 1, with the median particle size ($d_{50}$) of 16 μm.

The GGBS was activated by sodium hydroxides and sodium aluminate solutions, respectively (see the sample IDs in Table 2). The starting raw materials were mixed with the designed proportion in a Hobart mixer following the preparation procedure suggested by EN 196-1 [24]. The pastes were cast in the Ø 45 mm × 55 mm cylindrical plastic mold followed by vibration. All the pastes were sealed and cured at the ambient temperature until the specified curing ages.

The detailed information about the preparation of the used activators is presented as follows. The analytical grade sodium hydroxide pellets (99% purity) were dissolved in deionized water to prepare the sodium hydroxide (NH) solution for the Ref-NH samples, and the sodium hydroxide activator was prepared 24 h before applications. The analytical grade sodium aluminate pellets were dissolved in deionized water to prepare the sodium aluminate (NA) solution for the NA2 to NA4 samples, while the sodium aluminate activator was prepared 6 h before applications.

### 2.2. Testing methods

#### 2.2.1. Cold water extraction

The ground powder from pastes was utilized to measure the ions and the pH value of the pore solution by Cold water extraction (CWE) at specific curing ages (3, 7, 14, and 28 days). 50 g of powder was mixed with 50 g of deionized water and shaken for 5 mins (5-min leaching procedure) [25,26]. The suspension was then filtrated by a filter syringe.

**Table 1**
Chemical compositions and physical properties of GGBS.

| Chemical composition | GGBS (wt%) |
|---|---|
| MgO | 8.5 |
| $Al_2O_3$ | 13.2 |
| $SiO_2$ | 30.7 |
| $SO_3$ | 2.8 |
| $K_2O$ | 0.3 |
| CaO | 42.1 |
| $TiO_2$ | 1.6 |
| MnO | 0.4 |
| $Fe_2O_3$ | 0.4 |
| LOI[a] (1000 °C) | 1.323 |
| Particle density ($g/cm^3$) | 2.947 |
| BET Specific surface area ($m^2/g$) | 0.349 |

[a] LOI = loss on ignition at 1000 °C.

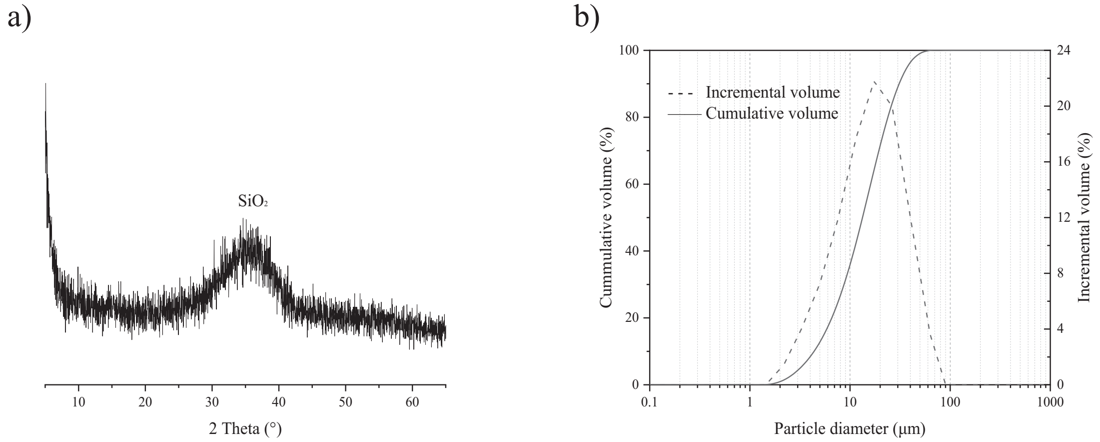

**Fig. 1.** a) X-ray diffractogram of GGBS; b) Particle size distribution of GGBS.

**Table 2**
Formulations of the paste samples.

| Sample ID | GGBS (g) | $NaAlO_2$ (wt %) | NaOH (wt %) | $Na_2O$/binder (wt %) | W/B[a] |
|---|---|---|---|---|---|
| NA2 | 100 | 5.288 | – | 2 | 0.4 |
| NA2.5 | 100 | 6.610 | – | 2.5 | 0.4 |
| NA3 | 100 | 7.933 | – | 3 | 0.4 |
| NA3.5 | 100 | 9.255 | – | 3.5 | 0.4 |
| NA4 | 100 | 10.577 | – | 4 | 0.4 |
| Ref-NH | 100 | – | 5.161 | 4 | 0.4 |

[a] W/B = water/binder mass ratio.

Previous studies showed no remarkable uptake of ions by the filter [26]. Finally, the rapid leachate was diluted 10 times with deionized water. The abstained diluted solutions were acidified with $HNO_3$ to prevent the precipitation, and then the solutions were analyzed for Al, Si, Mg, and other heavy metal ions using Inductively coupled plasma-optical emission spectrometry (ICP-OES). During the acidification $HNO_3$ process, the precipitation of $Al(OH)_3$ might appear. However, when sufficient $HNO_3$ is applied in the ICP testing solution, the precipitation disappears. Na and Ca were analyzed by diluted solution, using Ion chromatography (IC).

Based on the IC and ICP-OES results, the content of elements was calculated by Eq. (1)

$$X = [X]_{CWE} \bullet \frac{m_{w105} + m_{add}}{m_{sample}} \tag{1}$$

where X is the free cation content in the samples (mmol/L). $[X]_{CWE}$ is the concentration of the element in the filtrate obtained after CWE (mmol/L), determined by IC or ICP. $m_{w105}$ is the mass of evaporable water at 105 °C in the samples (see Table 3). $m_{add}$ is the mass of deionized water that is added during the 5-min rapid leaching process, and $m_{sample}$ is the mass of the sample (g).

$$\gamma[OH^-]_{CWE} = 10^{pH_{CWE}-14} \tag{2}$$

**Table 3**
Amount of evaporable water at 105 °C (i.e. free water) in the mortar samples 28 days after casting, $m_{w105}$ measured after oven-drying.

| | Before drying (g) | After drying (g) | $m_{w105}$ (g) | $\frac{m_{w105}+m_{add}}{m_{sample}}$ |
|---|---|---|---|---|
| NA2 | 49.97 | 38.85 | 11.12 | 1.22 |
| NA2.5 | 50.03 | 39.55 | 10.48 | 1.21 |
| NA3 | 49.91 | 40.12 | 9.79 | 1.20 |
| NA3.5 | 50.03 | 40.57 | 9.46 | 1.19 |
| NA4 | 50.05 | 40.21 | 9.84 | 1.20 |
| Ref-NH | 50.28 | 40.39 | 9.89 | 1.19 |

where $pH_{CWE}$ is the pH value in the filtrate obtained after CWE, γ is the activity coefficient at the testing moment. The activity coefficients can be calculated with the WATEQ Debye Hückel equation [27]. $[OH^-]_{CWE}$ is the $OH^-$ concentration calculated by the $pH_{CWE}$ after the CWE.

$$[OH^-] = [OH^-]_{CWE} \bullet \frac{m_{w105} + m_{add}}{m_{sample}} \tag{3}$$

where $[OH^-]$ is the real $OH^-$ concentration in the pore solution of the samples. Overall, the pH value of the pore solution could be calculated with Eq. (4), by combining the Eqs. (2) and (3).

$$pH = 14 + \frac{m_{w105} + m_{add}}{m_{sample}} \bullet \lg(\ pH_{CWE} - 14) \tag{4}$$

Using the CWE method to determine the pH and ions concentration has a limitation, but it has been proved that this method could obtain a relatively good estimate to predict the state of pore solution [25].

The measurement accuracy of alkali metal cations (i.e. $Na^+$, $K^+$, and $Ca^{2+}$) using CWE has been recommended in a previous study [25]. To evaluate the deviation of $Al(OH)_4{}^-$, $Si(OH)_4$, and $Mg^{2+}$ concentrations by CWE, a separate 5-min leaching test of raw GGBS powder was carried out under different pH values of the alkali leaching solution. The test results are shown in Table A7. When the pH is lower than 13, the metal ions of $Al(OH)_4{}^-$, $Si(OH)_4$, and $Mg^{2+}$ from GGBS will not influence the pore solution leaching results, therefore the deviation of ions' concentrations could be neglected in this study.

### 2.2.2. *pH value of pore solution at the early stage*

The pH value of the pore solution was determined by a pH meter in the slurry state of the pastes. The paste samples were cast in the plastic bottles, and the pH value of the slurry was determined at 5 min, 1 h, 3 h, 6 h, and 24 h.

### 2.2.3. *Isothermal calorimetry*

The heat flow of the samples activated by different activators was measured by isothermal calorimetry set at 20 °C (TAM AIR Calorimetry). It took about 5 min to prepare each testing sample externally. Then the samples were transferred to the ampules that were placed into the device sequentially. It should be noted that the values measured during the initial 45 min might slightly deviate as it takes time to stabilize the inner measurement environment. Because the introduction of ampules influences the inner temperature of the device [28]. The results were normalized by the mass of the solids.

### 2.2.4. *X-ray diffractometry*

X-ray diffractometry (XRD) was performed by using a Bruker D4 Phaser instrument with Co-$K_\alpha$ radiation (40 kV, 30 mA). The pressed powdered specimens were measured with a step size of 0.05° and a counting time of 1 s/step, from 10° to 90° 2θ.

### 2.2.5. Thermogravimetry

The thermogravimetric (TG) test was conducted by using an STA 449 F1 instrument, at a heating rate of 10 °C/min, to samples of ≈ 100 mg. Experiments were carried out from 40 °C to 1000 °C, and during the test process, $N_2$ was used as the carrier gas. Before the test, the pastes were ground to powder. Then the powder samples were immersed in 2-propanol for 24 h to stop the hydration process. Subsequently, the powder samples were dried in an oven at 60 °C for 3 days to remove the remaining free water and stored in the sealed plastic bag.

### 2.2.6. Fourier-transform infrared spectroscopy

Fourier-transform infrared spectroscopy (FTIR) analysis was performed using a Varian 670-IR spectrometer with a wavelength range of 400 to 4000 $cm^{-1}$ with a resolution of 1 $cm^{-1}$.

### 2.2.7. Nitrogen physisorption test

The nitrogen physisorption tests were conducted by TriStar II 3020, Micromeritics. The pore size distribution was determined by the Barett, Jonyer, and Halenda (BJH) method [29] from the desorption branch. Before the test, paste samples at the age of 28 days were ground to powder and the samples were immersed in the 2-propanol for 24 h to stop the reaction process, then dried to constant mass.

### 2.2.8. Chloride absorption test

An accelerated experimental approach was used to study the chloride absorption of SAAS samples. The chloride absorption tests were performed with 0.1 mol/L NaCl solution to the samples with a particle size <4 mm at the liquid to solid ratio of 2/1. In this accelerated chloride absorption test, the contact time between the solid material and the NaCl leachate was 24 h. 5 g of paste powder and 10 g of deionized water were placed in a plastic bottle, and 24-h shaking was performed on a shaking table (which is for the leaching test) with 200 rpm. After the shaking procedure, the eluate was filtrated through a 0.45 μm filter and analyzed for remaining chloride ions in the eluate by using Ion chromatography (IC). The ion chromatography (Dionex 1100) is equipped with an ion-exchange column AS9-HS (2 × 250 mm). The absorbed chloride ions could be calculated by comparing the original NaCl solution.

This non-standard leaching-absorption testing method is adopted from a previous study [30]. The hydrated gels and hydrotalcite in the reaction products can absorb the chloride ion during the shaking process. The results could generally evaluate the ability of chloride absorption of paste samples.

## 3. Results analysis

### 3.1. Evolution of pore solution

### 3.1.1. Variation of pH value

Previous studies indicated the significance of the pH value of pore solution on the reaction of AAMs [31–33]. According to Paudel et al. [34], the pH value of pore solution in the AAMs decreases with the curing ages, which is attributed to the process of reaction that consumed much of $OH^-$ in the pore solution. In this study, the evolution of the pH value of pore solution in the SAAS paste samples is obtained by the Cold Water Extraction (CWE) method. The sodium hydroxides activated GGBS was selected as a reference to compare with the sodium aluminate activated GGBS at the specific curing ages. Fig. 2 shows the pH value variation of pore solution in the SAAS paste samples at an early stage (5 mins, 1 h, 3 h, 6 h, and 24 h, by pH meter directly) and later stage (3, 7, 14, and 28 days, by CWE).

Fig. 2a) shows that all the samples exhibit, generally, the decreasing trend of pH value during the early stage, which is due to the dissolution of slag that consumes a large amount of $OH^-$. The Ref-NH shows the highest pH value while NA2 is the lowest among the samples, which represents the alkalinity of the samples. The pH at 6 h and 24 h of Ref-NH is tested by CWE because of the fast hardening of the paste which makes it impossible to test directly its pH with the pH meter. However, the pH changes of SAAS pore solutions exhibit a more gradual decrease than the Ref-NH, especially NA3.5 and NA4. The $NaAlO_2$ is a salt formed between a weak acid and a strong base, thus it has the capability to continue the hydrolysis of $OH^-$, which provides the buffering effect at the early stage of pH changes of the SAAS pore solution.

As can be seen in Fig. 2b), the Ref-NH shows the decrease of pH value along with the sample ages, ranging from 13.06 (3 days) to 12.53 (28 days). The cause of the pH decrease is that the formation of amorphous gel (C-A-S-H as mentioned in Section 3.3.1) and crystalline phases (Hydrotalcites and C-A-H as mentioned in Section 3.3.1) consumes the $OH^-$ continually in the pore solution. However, the pH value in the pore solution of SAAS paste samples shows a different trend. After decreasing at the early age, the pH value slightly increases from the age of 3 days to the age of 7 days, and then keeps relatively stable at further curing ages, around 12.7. The $NaAlO_2$ shows buffering effect at late stages in the pore solution of SAAS samples. Thereby, the pH value of the pore solution remains at different sample ages. Furthermore, it is worth mentioning that the higher the $Na_2O$ content in the SAAS matrix, the higher the initial pH value of the pore solution of SAAS pastes till the $Na_2O$ content of 3.5% (i.e. NA3.5). This can be explained by the limitation of $NaAlO_2$ hydrolysis.

### 3.1.2. Variation of ions

Fig. 3 presents the concentrations of Al, Si, Na, Ca, and Mg (hereafter

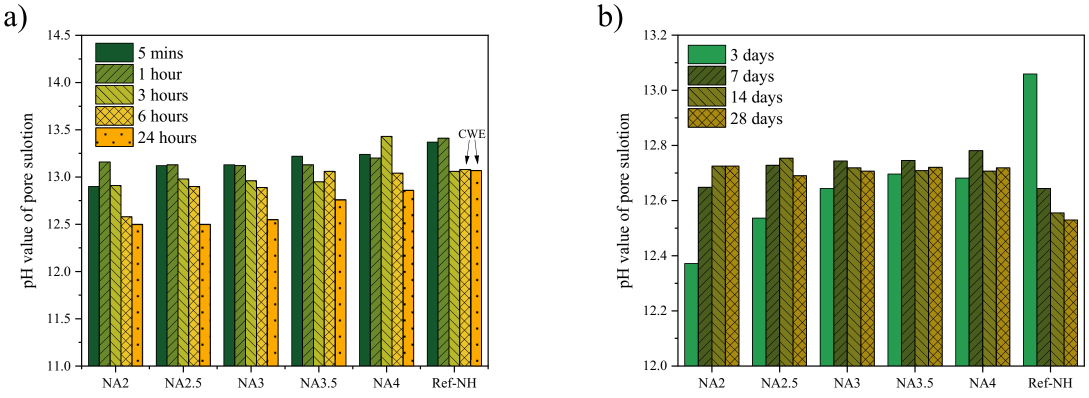

**Fig. 2.** Variation of pH value in the pore solution of AAMs: a) Early stage; b) After 3 days.

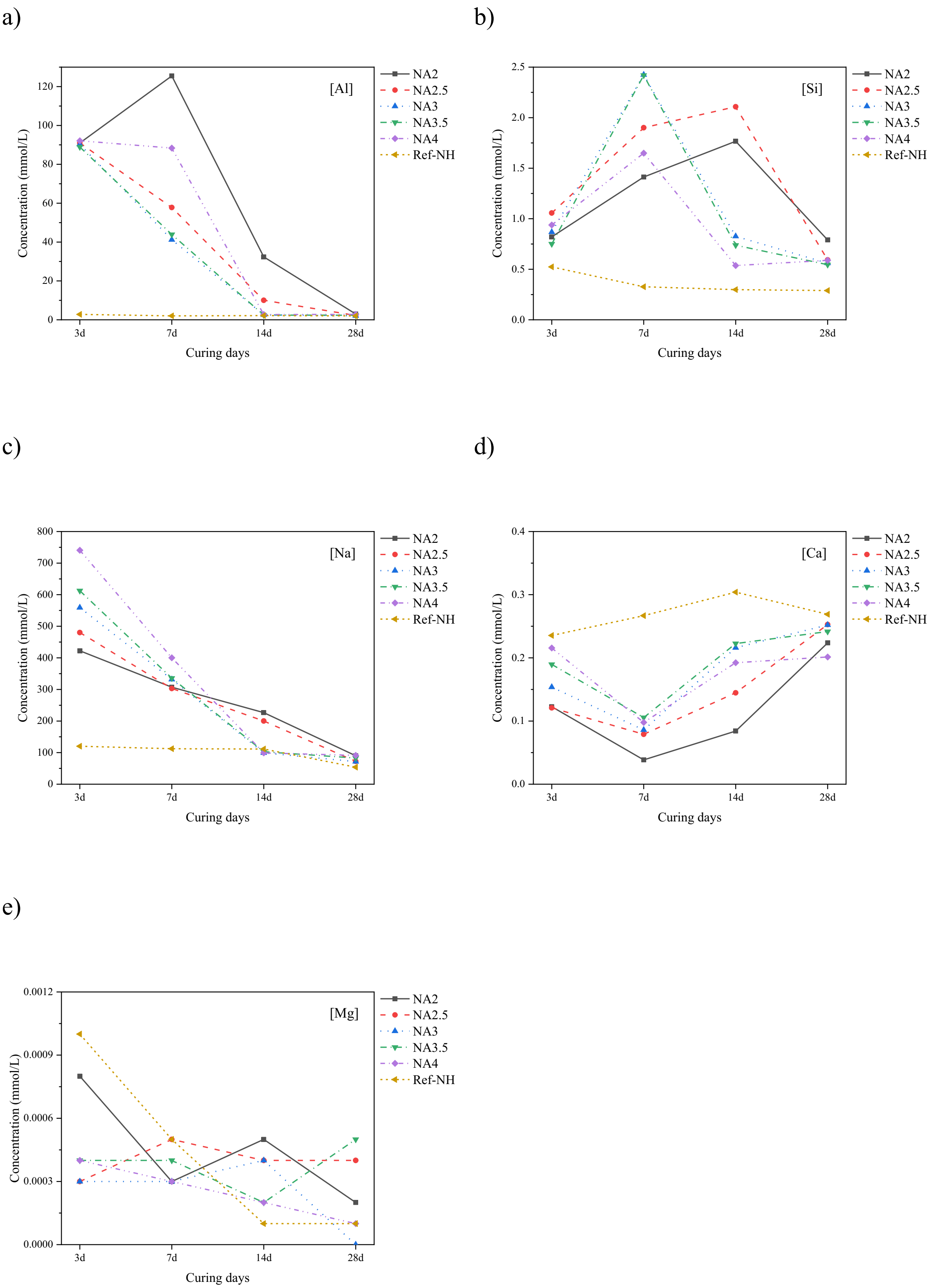

**Fig. 3.** Cation variation of pore solution in SAAS at different curing times: a) [Al]; b) [Si]; c) [Na]; d) [Ca]; e) [Mg].

denoted as [Al], [Si], [Na], [Ca], and [Mg] respectively) in the pore solution (unit mmol/L) of SAAS pastes as the function of time at 3, 7, 14 and 28 days. The detailed pore solution data are listed in Appendix Tables A1–A6. It is noted that [Na] and [Ca] were determined by the IC, while the rest of the ions were determined by the ICP-OES.

There is a strong variation of [Al] during the curing ages in NA samples, while the Ref-NH maintained the [Al] stably in the entire curing period (shown in Fig. 3a)). NA2 shows firstly an increasing trend of [Al] from 3 days to 7 days, then a remarkable decrease appeared after 7 days. The relatively lower pH value of pore solution in NA2 at 3 days, compared to that at the later curing period, results in the large content of unconsumed Al. In the meantime, the alkaline environment in the pore solution keeps breaking the Al-O bond from GGBS, consequently an increase in $Al(OH)_4^-$ is resulting. Subsequently, more and more $Al(OH)_4^-$ ions interact with $Si(OH)_4$ under the relatively higher pH value, compared to that at the early curing period, around 12.7, thus the [Al] declines with the curing ages. Thus NA2 shows a slow activation rate. However, unlike NA2, the [Al] keeps decreasing sharply in NA2.5, NA3, NA3.5, and NA4, attributed to the relatively higher pH values of the pore solution in these mixtures compared to that of NA2 that promotes the reaction between 3 and 7 days. However, NA2 remains insufficient pH of the pore solution in this period. According to the previous study [35], the increase of $Na_2O$ content (NaOH activated slag) will not lead to an obvious variation of [Al] in the pore solution. On the contrary, the increase of $Na_2O$ content in SAAS pastes directly introduces a great quantity of [Al] in the pore solution. The difference between NaOH and $NaAlO_2$ activated systems is obviously due to the diverse content of aluminate participation. At the same time, the Ref-NH shows that all the [Al], dissolved from GGBS, is under 3 mmol/L during the testing period. By the comparison of NA4 and Ref-NH, the difference of [Al] can be attributed to the extra aluminate content and pH value of the pore solution. With a higher pH environment of Ref-NH than that of NA4 before 3 days, the $Al(OH)_4^-$ is easier to be consumed to form gels (e.g. C-A-S-H gel) or crystalline phases (e.g. hydrotalcite) [36]. It is worth mentioning that the [Al] shows a similar concentration level after 28 days among the SAAS and reference samples, ranging from 2 to 3 mmol/L. This indicates that $Al(OH)_4^-$ in the pore solution is largely consumed during the activation process.

The [Si] of NA2 and NA2.5 shows a hill-like trend and the peaks of concentration appeared at 14 days. Likewise, the trends of [Si] in NA3, NA3.5, and NA4 are the same, whereas the peaks show at 7 days (shown in Fig. 3b)). The $Si(OH)_4$ in pore solution is completely originated from the GGBS, thereby the time to the peak reflects the rate of slag dissolution and the subsequent Si-O consumption, namely the activation process. Instantaneously, the [Si] in Ref-NH shows a low concentration ($< 0.53$ mmol/L) during the curing period, which represents the consummation of activation before 3 days. This is attributed to the high content of $Na_2O$ and pH value of pore solution in the NA samples that promotes gelation and crystallization.

There is a remarkable variation of [Na] during the testing period in all samples. The [Na] decreased remarkably with time among the samples (shown in Fig. 3c)). For the sodium aluminate activated system, the initial period of up to 3 days shows the extensively high [Na]. Simultaneously, the [Na] increased with the increase of $Na_2O$ content. However, comparing the NA4 with Ref-NH, the two mixtures with the equivalent $Na_2O$ content show a huge difference of [Na]. The $Na^+$ is consumed largely before 3 days in Ref-NH, while the SAAS samples show a delay in the activation of $Na^+$ with other ions in the following period (7 days to 14 days). During 7 days to 14 days, the [Na] of SAAS decreases to the concentration around 100 mmol/L, and the [Al] declines to the concentration below 3 mmol/L, at the same time, the [Si] remains at a low concentration. The changes of these ions reflect the process of activation between $Na^+$, $Al(OH)_4^-$, and $Si(OH)_4$.

The [Ca] of SAAS shows a valley-like trend along with the curing time, and all the bottoms appeared at 7 days (shown in Fig. 3d)). However, the [Ca] in Ref-NH increases with the curing time and reaches its peak (0.3040 mmol/L) at 14 days, and subsequently, decreases to 0.2689 mmol/L at 28 days. For SAAS samples, the $Ca^{2+}$ is remarkably consumed under the relatively stable pH environment along with the curing time to form Ca-based gels. Combining with [Al] and [Si], the $Ca^{2+}$ reacts with $Al(OH)_4^-$ before 14 days tremendously, which leads to a remarkable decrease of [Al] as well. After 14 days, the $Si(OH)_4$, $OH^-$, and $Na^+$ show lower values. The combination between $Si(OH)_4$, $OH^-$, $Na^+$, and $Ca^{2+}$ to form solid reaction products had dropped. It may lead to the compensation of $Ca^{2+}$ under the alkali environment in the pore solution. At the same time, the change of [Ca] may be also related to the alkalinity (pH) change of the pore solution. A higher alkalinity leads to a lower solubility of $Ca^{2+}$. Thereby, the valley-like trend of [Ca] appears in the pore solution, finally reaching a similar level among all samples. For the Ref-NH, the activation of $Ca^{2+}$ is mainly concentrated before 3 days, thus the $Ca^{2+}$ continually increases with the curing time. The low concentrations of [Al] and [Si] in Ref-NH after 3 days confirm that the activation has been transferred from a high rate of reaction to a low rate of it within the first 3 days. It may be associated with that the access of hydroxyl to the unreacted slag is inhibited by the reaction products around slag grains.

$Mg^{2+}$ is dissolved from GGBS under the alkaline environment, and the concentration ranges from 0 to 0.0012 mmol/L (shown in Fig. 3e)). The large content $Al(OH)_4^-$ reacts with $Mg^{2+}$ preferentially to form hydrotalcite, thereby the [Mg] remains at a low concentration during the curing time. The excessive $Al(OH)_4^-$ ions in the pore solution prevent the competition between $Si(OH)_4$ and $Mg^{2+}$ to form gels and hydrotalcite, respectively.

Overall, the [Al] shows a remarkably decreasing trend, generally, along the curing ages in the pore solution, which is associated with activation and the LDH formation process. Similarly, the [Na] declines with the curing time obviously, relating to the process of activation. The [Si] increases at early ages providing $Si(OH)_4$ and decreases after 7 days. The [Ca] decreases at the early ages reacting with dissolved $Si(OH)_4$, and rises after 7 days.

In addition, the [B], [Cu], [Fe], [Ga], [Li], [Se], and [V] showed lower than 0.2 mmol/L during the testing time, and details are shown in the Appendix Tables A1–A6.

### 3.2. Reaction kinetics

Fig. 4 shows the normalized reaction heat flow and cumulative reaction heat release of the SAAS pastes. A remarkably higher reaction heat flow and cumulative reaction heat release from the Ref-NH than the other SAAS pastes is observed. Generally, the higher the equivalent $Na_2O$ content in the SAAS, the higher the reaction heat flow, the higher cumulative reaction heat release, and the earlier reaction heat peak could be obtained.

As can be seen from Fig. 4 a), with the increasing equivalent $Na_2O$ content in the SAAS, the time to the first peak is decreased. However, the NA4 exhibits a delay at the time to the first peak compared to NA3.5. From NA2 to NA3.5, the pH value of the pore solution increases with the $Na_2O$ content at the early activation period, thus the time to the first peak decreases and the peak height raises. The first peak height of NA3.5 and NA4 are close to each other, which is in agreement with their similar pH value of pore solution. The first peak is mainly about the small amount of Calcium Aluminum Silicate Hydrate (C-A-S-H) gel and Calcium Aluminum Hydrate (C-A-H) formation (see Fig. 5 a)). The reason is that the pH environment around 13 (see Section 3.1.1) is suitable for gels formation at the beginning 6 h. The large amount of $OH^-$ is consumed subsequently, resulting in the pH decrease that slows down the reaction. Besides, the overall dissolution of elements in slag follows the equilibrium rule. Considering the low Ca concentration in the pore solution, a higher Al concentration in the pore solution leads to a lower Si concentration in the pore solution [37–39]. Therefore, Al competes with the dissolution of Si, resulting in the delay of time to the first peak in NA4 compared to NA3.5. Moreover, the extra Al hinders the activation at the early stage [40], and the total induction period of SAAS shows around 280 h. But the Al will be consumed after 14 days, which is also shown in Fig. 3, and the extra Al in NA4 could generate more zeolites and N-A-S-H gels (mix with zeolites formation). Because in this period, the $Na^+$ and $Al(OH)_4^-$ are consumed remarkably, thereby the long-term performance is improved by the increase of $Na_2O$ content. Although the extra aluminate extends the induction period of SAAS, there is still a large amount of $Si(OH)_4$ in the pore solution of SAAS, thereby the entire activation process of NA2.5 -NA4 finished after 14 days, and new phases are formed in this period. Because of the low alkaline environment, the steady stage of NA2 appeared after 14 days to reach the low rate of reaction state. Combining Sections 3.1.1 and 3.1.2, a stable pH at around

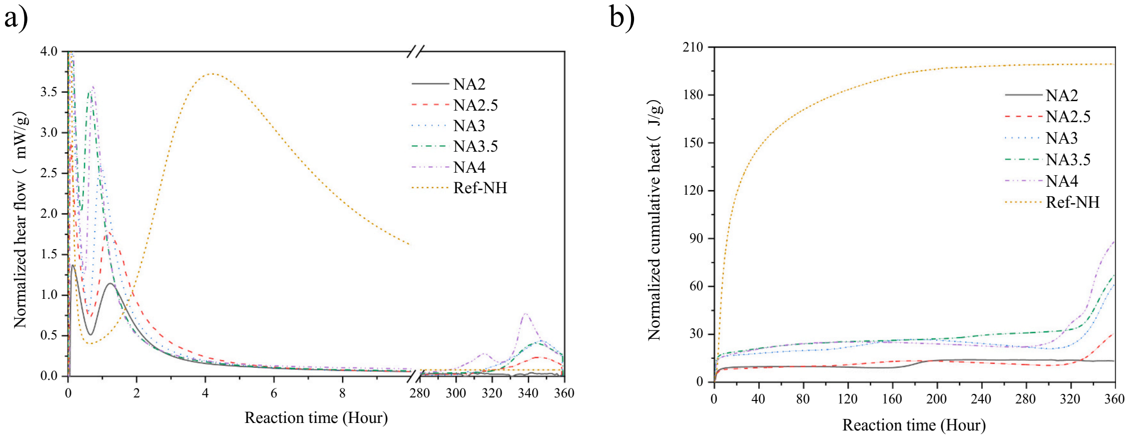

**Fig. 4.** a) Normalized reaction heat flow of SAAS; b) Cumulative reaction heat release of SAAS.

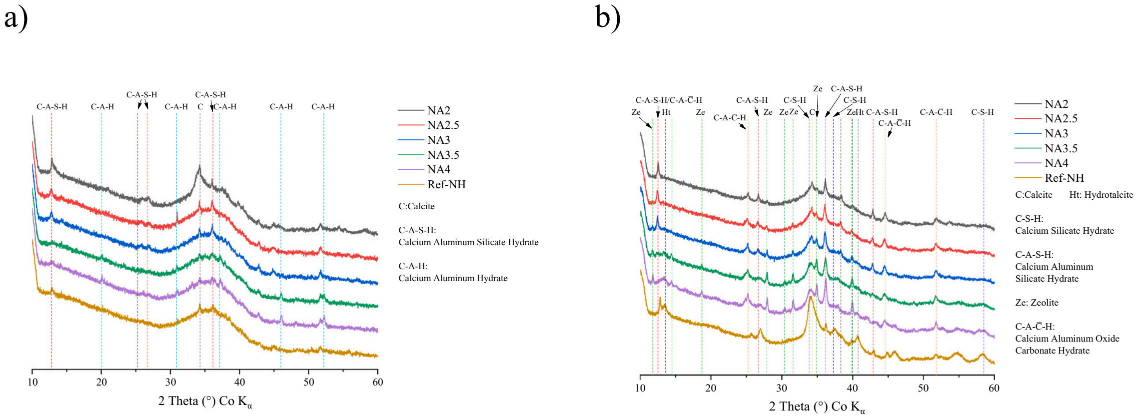

**Fig. 5.** XRD patterns of the SAAS pastes at a) 2 h, b) 28 days.

12.7 and [Al] around 3 mmol/L in the pore solution represent it reaching the low rate of reaction stages of SAAS. The [Al] of Ref-NH at 3 days is 2.7838 mmol/L, so it has already finished the activation process.

Fig. 4 b) illustrates the trend that with a higher aluminate content in the matrix, the cumulative heat release is increased. Specifically, the comparison between Ref-NH and NA4 shows that the cumulative heat release of NA4 pastes is remarkably lower than Ref-NH. Since the content of $Na_2O$ is the same, the difference in heat release can be attributed to the pH value of the early state in the pore solution. NA4 exhibits a relatively lower pH value than Ref-NH. So, the small amount of $OH^-$ ions in NA4 reflect the delay in the formation of early reaction products. Thereby the reaction heat is influenced by the pH to a great extent, showing low heat release at the early state. Further, the pH value of the pore solution is affected by the concentration of $Al(OH)_4^-$ in the SAAS pastes, resulting from the hydrolysis of $NaAlO_2$, which is the resource of the alkali in the SAAS pastes at early curing age. The higher the $NaAlO_2$ content, the higher pH at the early stage. Simultaneously, the difference of pH leads to the different concentrations of elements in the pore solution, it may also influence the heat release of the reaction at the early stage. Overall, lower heat release of NA4 is observed than that of Ref-NH.

## 3.3. Reaction products

### 3.3.1. X-ray diffraction

Fig. 5 a) and b) show the XRD patterns of the NaOH activated GGBS (reference sample) and SAAS pastes at 2 h and 28 days, respectively. The following phases are recognized at the first 2-h of reaction in Fig. 5 a): Calcium Aluminum Silicate Hydrate (C-A-S-H) (JCPDS-ICDD 00-016-0339), Calcium Aluminum Hydrate (C-A-H, JCPDS-ICDD 00-024-0217), and Calcite ($CaCO_3$, JCPDS-ICDD 01-086-2343). The dissolved $Ca^{2+}$ from GGBS reacts with excessive Al from the activator to form C-A-S-H and C-A-H, which leads to the fast coagulation of the paste samples. This phenomenon is similar to the false set caused by gypsum [41]. Along the early stage of the paste reaction, the pH environment decreases continually because of 1) the consumption of the $OH^-$ ions in the pore solution to form C-A-S-H and C-A-H, and 2) the dissolution of slag.

The following phases are recognized at 28 days in Fig. 5 b): Calcium Silicate Hydrate (C-S-H) (Tobermorite, JCPDS-ICDD 00-006-0010), Calcium Aluminum Silicate Hydrate (C-A-S-H) (JCPDS-ICDD 00-016-0339), Calcium Aluminum Oxide Carbonate Hydrate (C-A-$\overline{C}$-H) (JCPDS-ICDD 00-036-0129), Zeolite (Zeolite, JCPDS-ICDD 00-039-0222), Calcite ($CaCO_3$, JCPDS-ICDD 01-086-2343), and Hydrotalcite ($(Mg_{0.67}Al_{0.33}(OH)_2)(CO_3)_{0.165}(H_2O)_{0.48}$, JCPDS-ICDD 01-089-5434). The main reaction products of Ref-NH identified are C-S-H, C-A-S-H, Calcite, and Hydrotalcite, which is in agreement with our previous study [42]. The main reaction products of SAAS pastes are C-A-S-H, Zeolite, C-A-$\overline{C}$-H, Calcite, and Hydrotalcite. Due to the incorporation of the extra Al in the activator in NA2 ~ NA4, the activated systems favor to form C-A-S-H instead of C-S-H with the increasing Al/Si ratio [43,44]. Meanwhile, the excessive $Al(OH)_4^-$ in the activator promotes the reaction with the dissolved $Si(OH)_4$ from slag and $Na^+$ in the activator, leading to the formation of more zeolites and Sodium Aluminum Silicate Hydrates (N-A-S-H) gels [45]. From the XRD results (Fig. 5b)), the intensity of the zeolite peak becomes stronger when more Al is involved. At the same time, the peak intensity of C-A-S-H and C-A-$\overline{C}$-H decreases with the increase of sodium aluminate content. However, the intensity of zeolites shows an increasing trend, thus the N-A-S-H gel may also increase with the increase of zeolites. While in the Ref-NH, the dissolved $Al(OH)_4^-$ is from slag, reacting with the $Ca^{2+}$ and $Si(OH)_4$ to form C-S-H and C-A-S-H, because $Ca^{2+}$ has higher charges than $Na^+$ which is earlier to participate in the gel chain. In addition, with a higher content of sodium aluminate, the intensity of hydrotalcite shows an increasing tendency. Besides interacting with Ca, Na, and Si to form amorphous gels, Al also reacts with Mg to form extra hydrotalcite, and these two processes happen simultaneously.

To conclude, the increased sodium aluminate content promotes the formation of zeolites, N-A-S-H, and hydrotalcite, but decreases the formation of C-A-S-H. The small amount of calcite may be due to the slight carbonation of samples.

### 3.3.2. *Thermogravimetric analysis*

The results of thermogravimetric analysis (TGA) for the reference paste and SAAS pastes at 28-day curing time are presented in Fig. 6. As seen in Fig. 6a), the mass of samples is continuously decreasing during the temperature range from 40 °C to 1000 °C. Specifically, the main mass losses of bound water from C-S-H, C-A-S-H, and N-A-S-H gels were about 5.54%, 6.43%, 7.62%, 8.46%, 9.25%, and 8.18% in NA2 to Ref-NH, respectively, within the ranges of 100–300 °C [46–48]. The higher water losses in the ranges represented the higher content of gels formation, which is attributed to the higher $Al(OH)_4^-$ in the pore solution thanks to its promotion of gelation. As shown in Fig. 6a), the mass losses of second-largest peaks are about 1.42%, 1.66%, 1.81%, 2.12%, 2.34%, and 2.33% in NA2 to Ref-NH, respectively, within the ranges of 300–400 °C [47]. While the decomposition of hydrotalcite has two steps [16], the first one (150–250 °C) corresponds to the loss of the interlayer water, the second peak (250–450 °C) arises from the decomposition of the hydroxide layers and carbonate anion. Thus, the decomposition of the gels may overlap the first peak of hydrotalcite decomposition. Specifically, these second-largest peaks on DTG curves (Fig. 6b)) are assigned to the relative content of Mg-Al hydrotalcite decomposition. It is seen that the higher content of hydrotalcite appears with a higher aluminate content. According to Section 3.1.1, the pH environments of SAAS are closer than that of Ref-NH to the condition of hydrotalcite formation during the reaction period. It is worth mentioning that the main reaction period of Ref-NH is before 3 days and the pH value of the pore solution is around 13.1. While the reaction period of SAAS is between 7 days and 14 days, the pH value of the pore solution is around 12.5– 12.7. Meanwhile, the excessive $Al(OH)_4^-$ interacts with the $Mg^{2+}$ dissolved from GGBS to form more hydrotalcite. A slight content of calcite is found in all samples, which is due to the slight carbonation of the samples during the curing [49]. The TG results agree well with the observation of XRD analysis. The phases after 800 °C are caused by the recrystallization of new phases under high temperatures: 1) gehlenite (majority) is formed by the C-A-S-H under high-temperature heating [50]; 2) the small amount of Merwinite observed is originated from the activated GGBS [51]; 3) monticellite is also generated by the activated GGBS in a relatively low content [52] (see details in Fig. A1).

### 3.3.3. *Fourier-transform infrared spectroscopy*

The FTIR spectra of SAAS pastes, Ref-NH paste, and raw GGBS are presented in Fig. 7. The broadest peaks of SAAS pastes are located at 944 to 955 $cm^{-1}$, which are associated with the Si-O tetrahedra. The stretching vibrations of the Si-O tetrahedra represent the different number of bridging oxygen atoms. More specifically, the Si-O-Si bonds are due to the typical aluminosilicate chains containing C-S-H, C-A-S-H, or N-A-S-H type gels formed in the alkali activated GGBS. The reaction products tend to form Al-rich structures with the increasing aluminate content in the matrices. For all the spectrum, the bands at around 1646 and 3392 $cm^{-1}$ are attributed to the bending and stretching vibrations of bound water molecules, respectively. Similarly, the bands at around 666, 1415, and 1473 $cm^{-1}$ in all samples are due to the presence of carbonate with different vibration modes: $\nu_2[CO_3]^{2-}$ for 666 $cm^{-1}$, and $\nu_2[CO_3]^{2-}$ for 1415 and 1473 $cm^{-1}$ [53]. These carbonate phases are partly from hydrotalcite, partly from calcite, and partly from other carbonated phases, which is consistent with the XRD results (Fig. 5 b)).

Furthermore, a more distinctive effect of sodium aluminate on the main band shifts can be observed in the zoom-in graph of Fig. 7. An increase of the main band wavenumber is found in the higher sodium aluminate content in the matrices. It is known that the shifts of characteristic peaks of Si-O stretch are a notable feature of alkali activation, namely reaction, at around 950 $cm^{-1}$ [54]. A higher aluminate content increases the amount of available $Al(OH)_4^-$ at the entire reacting period, which has a major influence on the activation process, and it is also in agreement with the dissolved Al in the pore solution presented in Section 3.1.2. The $Al(OH)_4^-$ in the pore solution inhibits the dissolution process of $Si(OH)_4$, but the Si-O stretch is shifted because under the relatively high pH environment, the dissolved $Si(OH)_4$ in the pore solution would react with $Al(OH)_4^-$ immediately, forming the Al-rich geopolymer. Generally, the high $Al(OH)_4^-$ in the pore solution promotes the activation process.

## 3.4. *Microstructure*

Fig. 8 shows the pore size distribution of SAAS samples at 28 curing days by nitrogen sorption test. From the nitrogen sorption test, the mesopore (2–50 nm) and partial macropore (50– 200 nm) can be observed.

Fig. 8 a) represents the cumulative pore volume of SAAS paste samples. As can be seen, the total pore volume of samples declines with the increased content of sodium aluminate. Especially, mesopores are the primary pores in the microstructure. The NA2.5 ~ NA4 have a lower

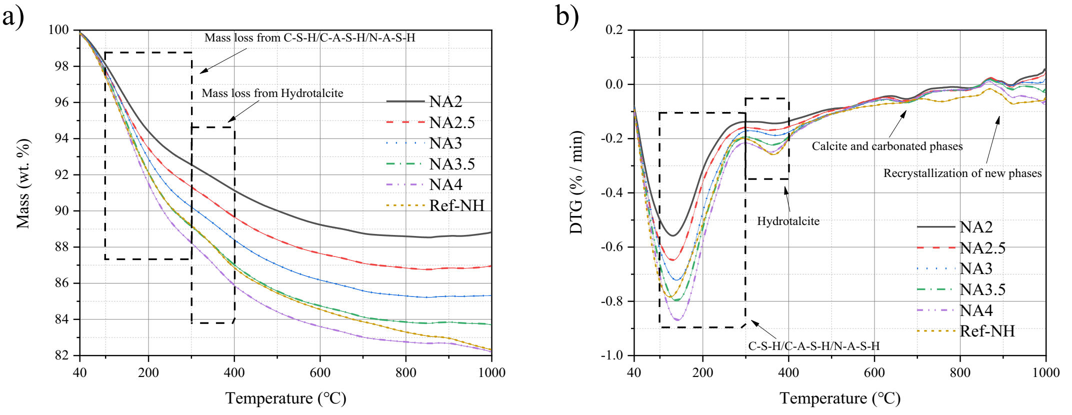

**Fig. 6.** a) Thermogravimetry (TG) curves of SAAS at 28 days; b) Differential thermogravimetry (DTG) curves of SAAS at 28 days.

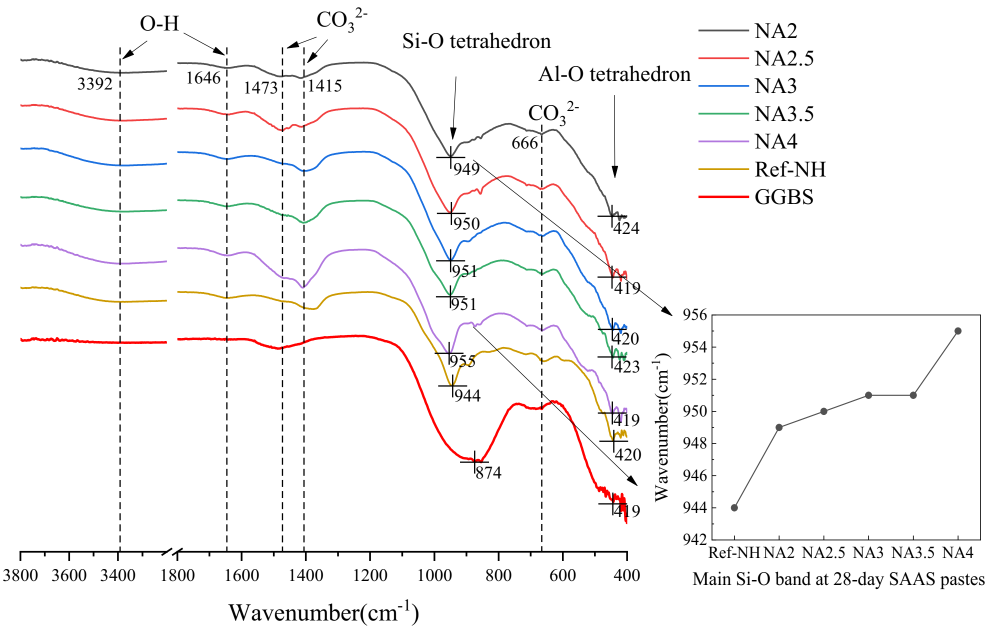

**Fig. 7.** FTIR spectrum of SAAS, Ref-NH, and GGBS.

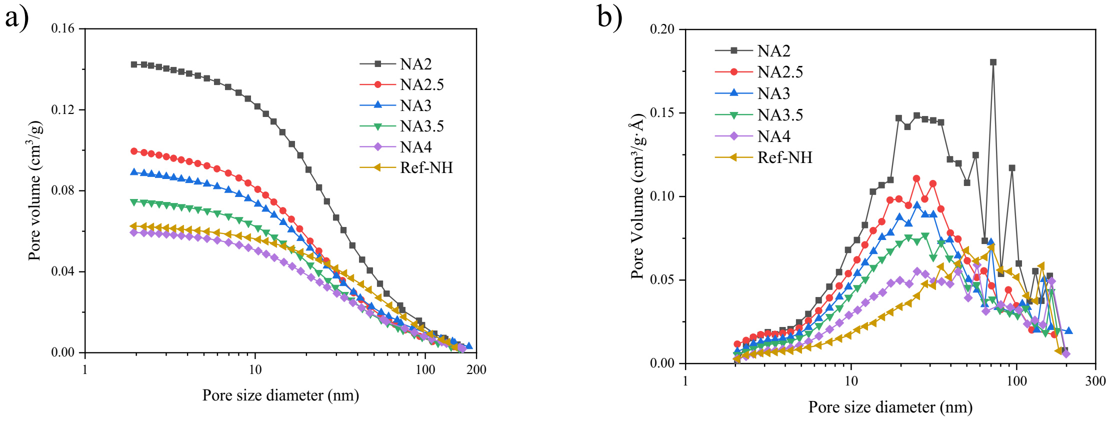

**Fig. 8.** a) BJH adsorption cumulative pore volume of SAAS at 28 days; b) Pore size distribution of SAAS from BJH adsorption dV/dlog(w) pore volume at 28 days.

cumulative pore volume (partial mesopore ranging from 27 to 50 nm) than the Ref-HN, while the cumulative pore volume of NA2 is higher than the reference sample. For NA2.5 to NA4, the refinement of pore structure is attributed to the higher amounts of gels (C-A-S-H / N-A-S-H) filling in the capillary pores, which is also in line with the TG results. Thereby, the matrices tend to be more compacted and have a higher capacity to prevent water penetration and ion transport, e.g. chloride ion.

The pore size distribution of SAAS is illustrated in Fig. 8 b). Among the samples, the peaks of the void are concentrated at around 20– 30 nm, namely mesopores. It is attributed to the gelation of C-A-S-H/N-A-S-H, the gel grew to intertwine and crosslinked to fill the mesopores, which results in the decrease of the volume of mesopores with the higher sodium and aluminate contents. While the NA2 has the highest peak at around 70 nm, the second peak is consistent with the other samples. From Sections 3.1.1 and 3.1.2, the low alkalinity of NA2 and slow consumption of $Al(OH)_4^-$ in the pore solution resulted in the low content of gelation, consequently, poor microstructure. The content of gel formation is relatively lower than the others, therefore increasing the total pore volume in the matrix.

### 3.5. *Chloride absorption*

Fig. 9 a) presents the chloride concentration in the remaining solution after 24-h leaching of the SAAS pastes, and the original leaching liquid is the 0.1 mol/L NaCl solution. Fig. 9 b) presents the normalized content of chloride absorption by the SAAS pastes, corresponding to the results shown in Fig. 9 a).

As seen in Fig. 9 a), all the samples show a remarkable decrease of $Cl^-$ concentration in the remaining liquid, compared to the reference NaCl solution. Similarly, the NA3, NA3.5, and NA4 illustrate the distinctively high chloride absorption at 1.69, 1.87, and 1.90 mg chloride/g paste, respectively, with an increase up to 32.03%, 46.09%, and 48.44%, compared to the Ref-NH (1.28 mg chloride/g paste). Compared to NA3, the NA3.5 and NA4 have higher C-A-S-H/N-A-S-H contents, they show a noticeable increase of chloride absorption than that of NA3 up to 10.65% and 12.43%, respectively. Moreover, the content of hydrotalcite in NA4 is also higher than that of Ref-NH, which leads to a higher ability to absorb chloride ions by both ion exchange and surface stabilization. Besides, the less content of mesopore, the higher chloride resistance generally [9], thereby the lower volume of part mesopore (27– 50 nm) in NA3, NA3.5, and NA4 than Ref-NH improve the chloride absorption.

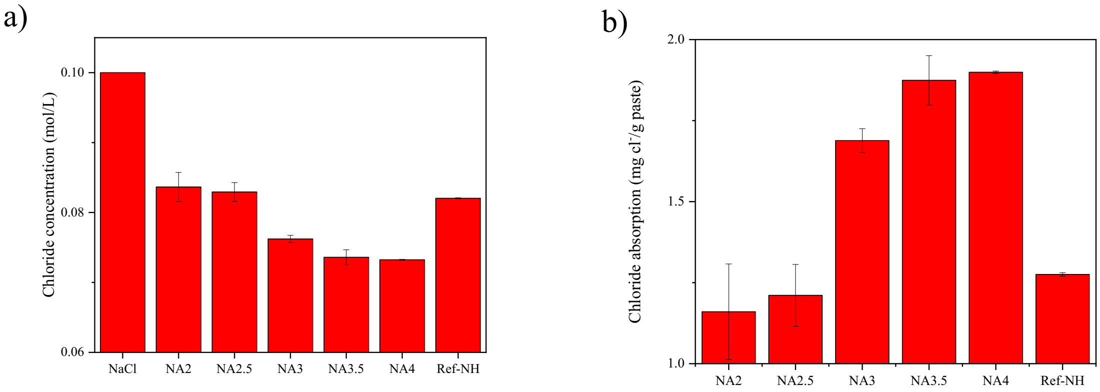

**Fig. 9.** a) Chloride concentration in the remaining solution after 24-hour shaking of the SAAS pastes; b) Contents of chloride absorption in the SAAS pastes.

However, the NA2 and NA2.5 show slightly lower chloride absorption at 1.16 and 1.21 mg chloride/g paste, respectively, lower than the Ref-NH up to 9.38% and 5.47%, respectively. Simultaneously, the content of gels and hydrotalcite of NA2 and NA2.5 are relatively lower than the Ref-NH, which decreases the chloride absorption.

## 4. Discussions

Understanding the changes in the pore solution upon different ions and pH is critical regarding understanding the mechanisms of LDH and gels formation along the curing period. In this paper, the role of $Al(OH)_4^-$ provided by sodium aluminate was investigated to understand how it influences the formation of in-situ formed LDH and gels. The CWE was used to determine the dynamic ion changes (including Al, Si, Na, Mg, Ca, etc.) in the pore solution.

### *4.1. Effect of $Al(OH)_4^-$ on LDH formation*

### *4.1.1. Comparison of $Al(OH)_4^-$ profiles from CWE with LDH profiles from TGA*

In Fig. 10, the $Al(OH)_4^-$ profiles determined by CWE at 3, 7, 14, and 28 curing days are compared to the LDH profiles at 28 curing days determined by TGA. The concentration of $Al(OH)_4^-$ in Ref-NH remains at a low level from 3 days to 28 days, thus the dissolved $Mg^{2+}$ reacts with dissolved $Al(OH)_4^-$ from GGBS to form the LDH. The concentration of $Al(OH)_4^-$ in the SAAS pastes exhibits a declining trend with the curing time, especially after 14 days. With a higher content of $Al(OH)_4^-$ in the pore solution of SAAS, more LDHs are formed, which is consistent with the declining trend of $Mg^{2+}$ concentration. It can be seen that the LDH formation is controlled by the content of available $Al(OH)_4^-$ in the pore solution. The formations of gel, $Al(OH)_4^-$ interacting with $Si(OH)_4$, and LDH, $Al(OH)_4^-$ interacting with $Mg^{2+}$, show no priority under the high amount of $Al(OH)_4^-$ in the pore solution. Here, the $Al(OH)_4^-$ in NA2 exhibits the increasing trend before 7 days, which is different from the other mixes. Because the Al dissolved from slag may not be consumed under the low pH environment of the NA2 pore solution, an increase of $Al(OH)_4^-$ is observed, but the other pastes have sufficient alkalis to consume $Al(OH)_4^-$ forming LDH, zeolites, and gels.

From this aspect, the key point promoting the in-situ formed LDH is to control the competition between $Mg^{2+}$ and $Si(OH)_4$ to react with $Al(OH)_4^-$. In Fig. 11, the mechanism of $NaAlO_2$ activated slag is proposed based on the dynamic $Al(OH)_4^-$ concentration in the pore solution to promote the LDH and gels formation. In the $NaAlO_2$ activated slag, the extra free $Al(OH)_4^-$ from the activator prevents the competition between $Mg^{2+}$ and $Si(OH)_4$ reacts with $Al(OH)_4^-$ in the pore solution. Consequently, the LDH ($Mg^{2+}$ reacts with $Al(OH)_4^-$) and gels ($Si(OH)_4$ reacts with $Al(OH)_4^-$) are generated simultaneously. It is shown that the high concentration of $Al(OH)_4^-$ in the pore solution avoids the competitive mechanism, in other words, to achieve the promotion of in-situ formed LDH. While in the NaOH activated slag, the $Al(OH)_4^-$ dissolves from slag, which will react with $Si(OH)_4$ and $Ca^{2+}$ (also dissolved from slag) to form C-A-S-H, thus $Al(OH)_4^-$ might be insufficient to react with $Mg^{2+}$ to form LDH at the same time.

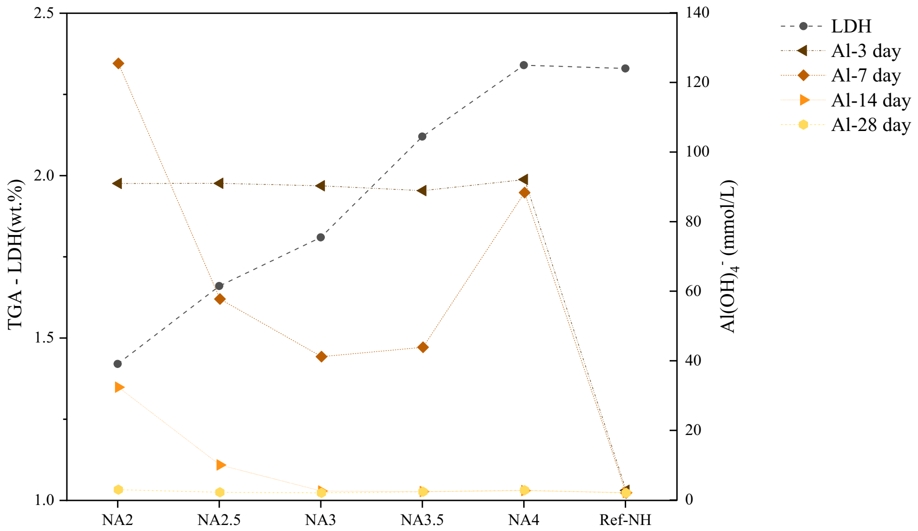

**Fig. 10.** The comparison of $Al(OH)_4^-$ profiles (3, 7, 14, 28 days) from CWE with LDH profiles (28 days) from TGA.

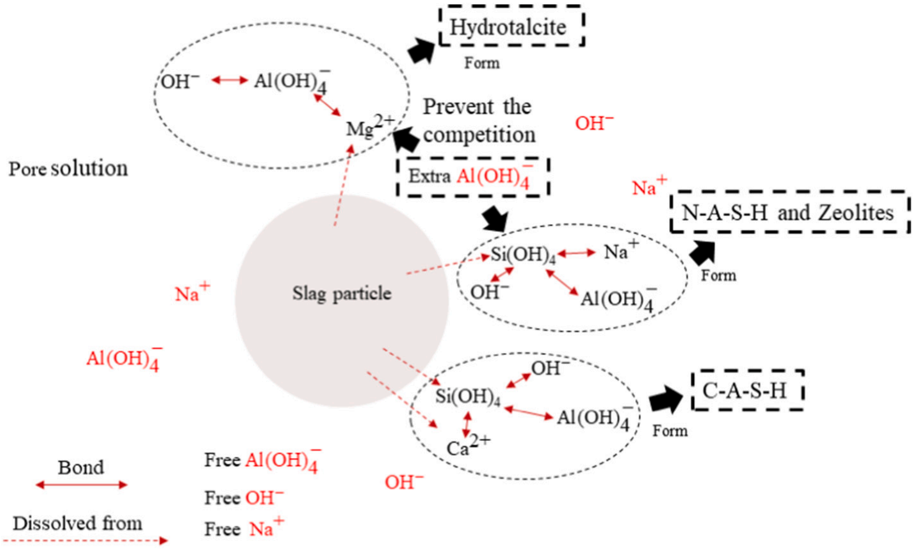

**Fig. 11.** Mechanism of $NaAlO_2$ activated slag.

### 4.1.2. Comparison of the $Mg^{2+}$ and $Al(OH)_4^-$ profiles with pH in pore solution from CWE on LDH formation

In Fig. 12, the concentrations of the $Mg^{2+}$ and $Al(OH)_4^-$ are presented with the pH value in the pore solution. The NA3.5 and NA4 show the similar pH value and the concentrations of $Mg^{2+}$and $Al(OH)_4^-$ at the entire curing times, while the NA4 shows that more $Mg^{2+}$and $Al(OH)_4^-$ have been consumed to form LDH and gels at 28 days. Moreover, NA2 has a low pH value of around 12.5, while NA4 shows a pH of about 12.7 during the entire reaction period. Both the pH values of NA2 and NA4 are relatively lower than that of the Ref-NH at the early stage of the reaction. LDH is observed in the Ref-NH at the early state, however, the LDH in NA2 and NA4 is shown only after 14 days.

It should be noted that the solubility of $Mg^{2+}$ is another primary reason for the LDH formation. For synthesis of pure Mg-Al LDH in carbonate form, a relatively lower pH (e.g. 9–11) is often reported [55]. However, in this work, a sufficient pH environment is firstly needed to dissolve the raw materials for the subsequent activation reaction. It is observed that the $Al(OH)_4^-$ favors reacting with $Mg^{2+}$ to form LDH under the pH of about 12.5– 12.7 in this study.

To discuss it further, the Mg/Al molar ratio shows an increasing trend along with curing time in SAAS, which is attributed to the pH increase in the matrix and the available $Mg^{2+}$ is increased and favors to form more LDH in the suitable pH environment. The in-situ formed LDH may also be influenced by the changes of the Mg/Al molar ratio in the pore solution. The extra $Mg^{2+}$ further accelerates the LDH formation and the process of reaction in SAAS systems.

### 4.2. Effect of pH, $Na^+$, $Ca^{2+}$, $Si(OH)_4$ and $Al(OH)_4^-$ on C(N)-A-S-H formation

Fig. 13 represents the concentrations of $Na^+$, $Ca^{2+}$, $Si(OH)_4$, and $Al(OH)_4^-$ with pH value in the pore solution from CWE profile, comparing with C(N)-A-S-H formation from TGA results. The most obvious discrepancy is the two different competing groups of ions 1) $Na^+$ and

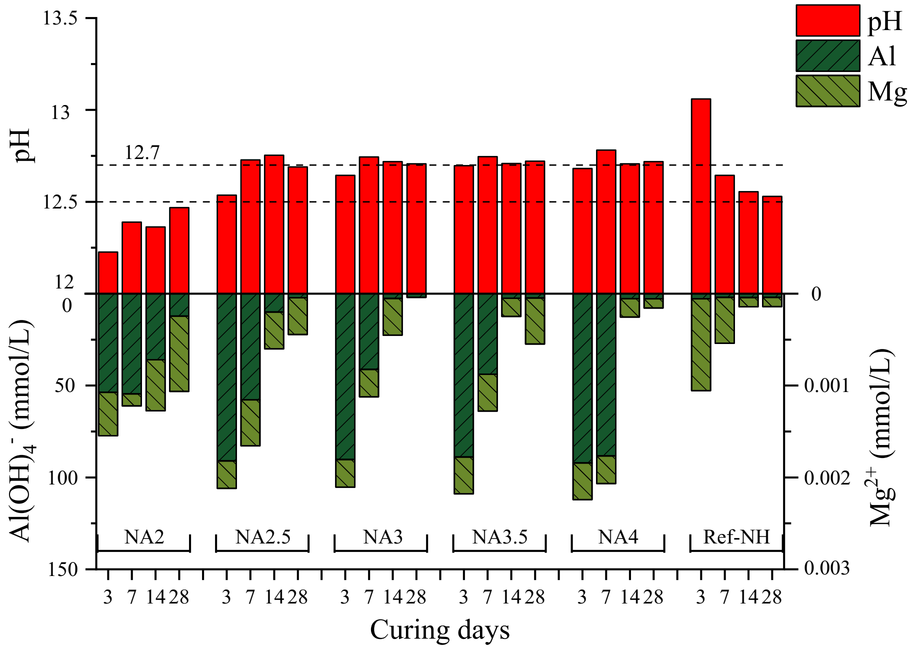

**Fig. 12.** The variation of pH, $Mg^{2+}$ and $Al(OH)_4^-$ in the pore solution.

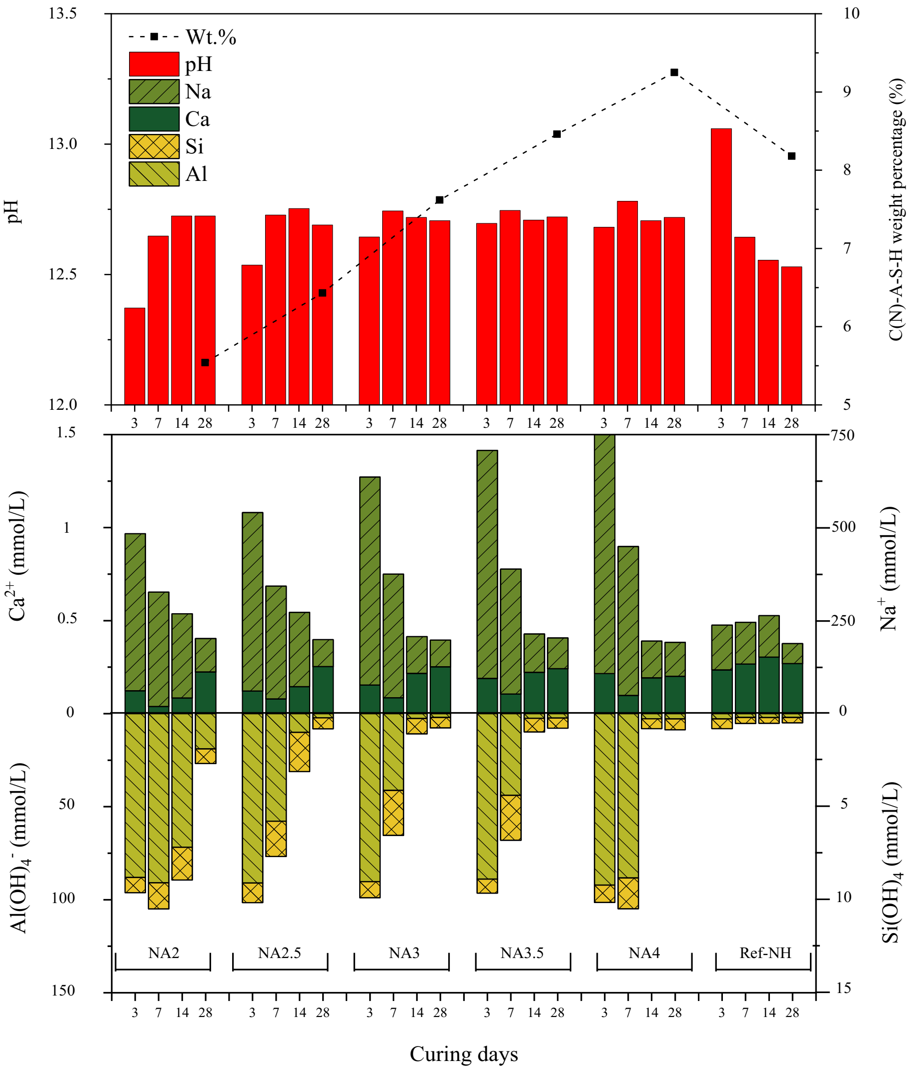

**Fig. 13.** The variation of pH, $Na^+$, $Ca^{2+}$, $Si(OH)_4$, and $Al(OH)_4^-$ in the pore solution and C(N)-A-S-H formation.

$Ca^{2+}$, 2) $Si(OH)_4$, and $Al(OH)_4^-$. The molar ratio of $Na^+/Ca^{2+}$ continually decreases with the curing age. Simultaneously, the molar ratio of $Si(OH)_4/Al(OH)_4^-$ gradually increases to the same level at the end of curing age, around 0.15 to 0.27. Compared to the C(N)-A-S-H formation, the Al participates mostly in the reaction, and the amorphous gels increase obviously with the content of $Na^+$ and $Al(OH)_4^-$. It is worth mentioning that the pH conditions of zeolite and N-A-S-H growth ranged from 9.5 to higher than 12, therefore the pH environment of all SAAS samples is suitable for the formation of zeolite and N-A-S-H gel. Meanwhile, the stable pH values and tremendous $Na^+$ content in SAAS samples lead to the formation of more zeolite, as observed in the XRD patterns. Among the samples, the $Na^+/Ca^{2+}$ ratio and $Si(OH)_4/Al(OH)_4^-$ ratio change obviously between 7 days and 14 days, which represents the formation of C(N)-A-S-H at this period in the sodium aluminate activating system. The extra $Na^+$ and $Al(OH)_4^-$, especially $Al(OH)_4^-$ ions, dominate the reaction in the entire testing age. The C-A-S-H and N-A-S-H gels are promoted by the extra available $Al(OH)_4^-$ in the pore solution to undergo the reaction of SAAS. Moreover, when the pH environment is sufficient for the gelation, the extra Al in the pore solution inhibits the dissolved Si from GGBS, so it can postpone the partial Al reacts with Si up to 7 to 14 days, while the reaction of the sodium hydroxide system has reached the low rate of reaction before 3 days. Eventually, the ratio of $Si(OH)_4/Al(OH)_4^-$ ended at around 0.25 (average results), with a low concentration of $Si(OH)_4$ (around 0.62 mmol/L) and $Al(OH)_4^-$ (around 2.49 mmol/L), which indicates it reaching a low rate of reaction.

Fig. 14 proposes the process of sodium aluminate activation, the pH environment of the pore solution has a significant effect on the final products. In the beginning, the pH value of the pore solution is relatively low, the $Ca^{2+}$ is easier to keep soluble in the pore solution. Consequently, dissolved $Ca^{2+}$ participates in the activation process with $Si(OH)_4$, $Al(OH)_4^-$, and $OH^-$, thus the C-A-S-H is generated. However, the amount of free $Ca^{2+}$ declines in the pore solution when the pH rises higher than 12.5. It is associated with its pH-dependent solubility. Then the $Na^+$ is captured by the $Si(OH)_4$, $Al(OH)_4^-$, and $OH^-$ forming N-A-S-H gel and zeolite. The synergistic effect of pH, $Na^+$, $Ca^{2+}$, and $Al(OH)_4^-$, transforms the final products from C-A-S-H dominated to N-A-S-H dominated in the SAAS system. Eventually, the N-A-S-H gel and zeolite became the dominant reaction products in the SAAS system.

## 5. Conclusions

This study attempts to deepen the understanding of sodium aluminate activated ground granulated blast-furnace slag (SAAS), with the aim of enhanced chloride absorption ability by promoting the in-situ formed LDHs through the alkali activation. This study shows that the sodium aluminate activator provides a relatively low pH environment and extra $Al(OH)_4^-$, to facilitate the in-situ formation of hydrotalcites

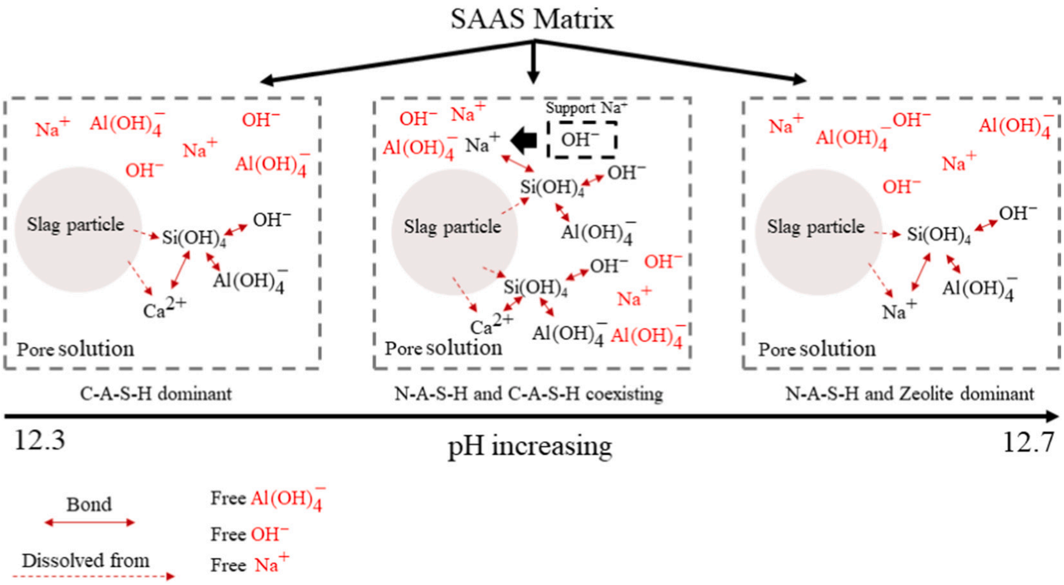

**Fig. 14.** Synergistic effect of pH, $Na^+$, $Ca^{2+}$, $Si(OH)_4$, and $Al(OH)_4{}^-$ in the pore solution of SAAS.

(LDHs). Moreover, the low pH activation shows the potential to tackle the issue of the high pH of the AAMs to human health which significantly limits its engineering applications. The following detailed conclusions can be drawn:

- The sodium aluminate activated slag results in the preferred in-situ formed LDHs. Simultaneously, with a higher sodium aluminate content, the content of gels in the SAAS is promoted. Thereby, the chloride binding capacity is enhanced by the promoted generation of reaction products (LDHs and gels).
- The sodium aluminate provides the extra $Al(OH)_4{}^-$ in the pore solution, which lessens the competition between $Si(OH)_4$, and $Mg^{2+}$ capturing $Al(OH)_4{}^-$. It confirms the hypothesis of this study that the extra Al could promote the content of in-situ formed LDHs and gels simultaneously.
- The proposed low pH activation of SAAS between 12.5 and 12.7 is desired to promote the in-situ formation of Mg-Al LDH. Along with the curing ages, the increase of pH value in the pore solution of SAAS transfers the primary reaction products from C-A-S-H to N-A-S-H and zeolites.
- The ratio of $Si(OH)_4$/ $Al(OH)_4{}^-$, stabilizes at around 0.25, with a low concentration of $Si(OH)_4$ (around 0.62 mmol/L) and $Al(OH)_4{}^-$ (around 2.49 mmol/L), representing the SAAS reaching the low rate of reaction state.

Nevertheless, slow reactions of the sodium aluminate activated slag are observed, which is due to the low alkalinity and high $Al(OH)_4{}^-$ concentration in the pore solution of the system. Exploring approaches to deal with the slow reaction rate of SAAS would be of scientific and practical interest in terms of the in-situ formation of LDHs.

## CRediT authorship contribution statement

Tao Liu: Methodology; Investigation; Data curation; Formal analysis; writing-original draft.

Qingliang Yu: Conceptualization; Methodology; Supervision; Project administration; Writing – Review Editing.

H.J.H. Brouwers: Supervision; Writing – Review Editing.

## Declaration of competing interest

The authors declare that they have no known competing financial interests or personal relationships that could have appeared to influence the work reported in this paper.

## Acknowledgment

This study is supported by the National Natural Science Foundation of China (Grant No. 52178246), the China Scholarship Council (Grant No. 201907720114) and Eindhoven University of Technology. Special thanks are expressed to A.C.A. Delsing for her help with the IC and ICP analyses.

## Appendix A

The pore solution composition data of Ref-NH, NA2, NA2.5, NA3, NA3.5, NA4 are listed in respectively.

**Table A1**
Ions concentration of NA2 at different function times (mmol/L)

| Samples | Na | Ca | Si | Al | B | Cu | Fe | Ga | Li | Mg | Se | V |
|---|---|---|---|---|---|---|---|---|---|---|---|---|
| NA2 3d | 422.3280 | 0.1227 | 0.8206 | 90.9544 | 0.0647 | 0.0007 | 0.0454 | 0.0135 | 0.0049 | 0.0008 | 0.0030 | 0.0110 |
| NA2 7d | 307.2342 | 0.0385 | 1.4125 | 125.4716 | 0.0660 | 0.0003 | 0.0312 | 0.0129 | 0.0037 | 0.0003 | 0.0024 | 0.0143 |
| NA2 14d | 226.6478 | 0.0841 | 1.7661 | 32.3877 | 0.1070 | 0.0002 | 0.0821 | 0.0095 | 0.0030 | 0.0005 | 0.0022 | 0.0193 |
| NA2 28d | 90.0473 | 0.2237 | 0.7905 | 2.9636 | 0.0882 | 0.0001 | 0.0127 | 0.0013 | 0.0076 | 0.0002 | 0.0006 | 0.0025 |

**Table A2**
Ions concentration of NA2.5 at different function times (mmol/L)

| Samples | Na | Ca | Si | Al | B | Cu | Fe | Ga | Li | Mg | Se | V |
|---|---|---|---|---|---|---|---|---|---|---|---|---|
| NA2.5 3d | 480.1467 | 0.1209 | 1.0572 | 91.0072 | 0.0757 | 0.0002 | 0.0438 | 0.0154 | 0.0044 | 0.0003 | 0.0032 | 0.0141 |
| NA2.5 7d | 303.1695 | 0.0790 | 1.9007 | 57.7767 | 0.1152 | 0.0000 | 0.0906 | 0.0121 | 0.0028 | 0.0005 | 0.0025 | 0.0220 |
| NA2.5 14d | 200.0539 | 0.1447 | 2.1079 | 10.0428 | 0.1597 | 0.0000 | 0.0562 | 0.0071 | 0.0031 | 0.0004 | 0.0015 | 0.0161 |
| NA2.5 28d | 72.4681 | 0.2527 | 0.5925 | 2.2263 | 0.0574 | 0.0000 | 0.0060 | 0.0008 | 0.0082 | 0.0004 | 0.0005 | 0.0015 |

**Table A3**
Ions concentration of NA3 at different function times (mmol/L)

| Samples | Na | Ca | Si | Al | B | Cu | Fe | Ga | Li | Mg | Se | V |
|---|---|---|---|---|---|---|---|---|---|---|---|---|
| NA3 3d | 559.2362 | 0.1537 | 0.8682 | 90.2738 | 0.0927 | 0.0001 | 0.0418 | 0.0175 | 0.0033 | 0.0003 | 0.0037 | 0.0172 |
| NA3 7d | 331.9159 | 0.0859 | 2.4244 | 41.1940 | 0.1435 | 0.0001 | 0.0712 | 0.0125 | 0.0028 | 0.0003 | 0.0026 | 0.0267 |
| NA3 14d | 99.0634 | 0.2161 | 0.8261 | 2.5922 | 0.0774 | 0.0001 | 0.0132 | 0.0013 | 0.0073 | 0.0004 | 0.0007 | 0.0023 |
| NA3 28d | 71.4253 | 0.2521 | 0.5604 | 2.0620 | 0.0519 | 0.0001 | 0.0061 | 0.0008 | 0.0098 | 0.0000 | 0.0005 | 0.0015 |

**Table A4**
Ions concentration of NA3.5 at different function times (mmol/L)

| Samples | Na | Ca | Si | Al | B | Cu | Fe | Ga | Li | Mg | Se | V |
|---|---|---|---|---|---|---|---|---|---|---|---|---|
| NA3.5 3d | 612.6617 | 0.1896 | 0.7509 | 88.9156 | 0.1102 | 0.0001 | 0.0390 | 0.0186 | 0.0029 | 0.0004 | 0.0041 | 0.0196 |
| NA3.5 7d | 335.7975 | 0.1055 | 2.4191 | 43.8903 | 0.1657 | 0.0001 | 0.0671 | 0.0137 | 0.0026 | 0.0004 | 0.0027 | 0.0300 |
| NA3.5 14d | 102.8402 | 0.2226 | 0.7378 | 2.4238 | 0.0778 | 0.0002 | 0.0133 | 0.0013 | 0.0092 | 0.0002 | 0.0008 | 0.0023 |
| NA3.5 28d | 82.8333 | 0.2417 | 0.5455 | 2.3718 | 0.0596 | 0.0001 | 0.0085 | 0.0009 | 0.0137 | 0.0005 | 0.0006 | 0.0014 |

**Table A5**
Ions concentration of NA4 at different function times (mmol/L)

| Samples | Na | Ca | Si | Al | B | Cu | Fe | Ga | Li | Mg | Se | V |
|---|---|---|---|---|---|---|---|---|---|---|---|---|
| NA4 3d | 740.7523 | 0.2156 | 0.9378 | 92.1152 | 0.1379 | 0.0000 | 0.0425 | 0.0220 | 0.0026 | 0.0004 | 0.0047 | 0.0239 |
| NA4 7d | 400.3221 | 0.0978 | 1.6493 | 88.3565 | 0.1705 | 0.0001 | 0.0642 | 0.0177 | 0.0026 | 0.0003 | 0.0033 | 0.0331 |
| NA4 14d | 99.1647 | 0.1923 | 0.5369 | 2.6865 | 0.0712 | 0.0000 | 0.0107 | 0.0014 | 0.0109 | 0.0002 | 0.0008 | 0.0022 |
| NA4 28d | 91.1295 | 0.2014 | 0.5889 | 2.8065 | 0.0614 | 0.0000 | 0.0071 | 0.0011 | 0.0174 | 0.0001 | 0.0007 | 0.0014 |

**Table A6**
Ions concentration of Ref-NH at different function times (mmol/L)

| Samples | Na | Ca | Si | Al | B | Cu | Fe | Ga | Li | Mg | Se | V |
|---|---|---|---|---|---|---|---|---|---|---|---|---|
| Ref-NH 3d | 120.2818 | 0.2354 | 0.5234 | 2.7838 | 0.0750 | 0.0001 | 0.0319 | 0.0001 | 0.1948 | 0.0010 | 0.0028 | 0.0032 |
| Ref-NH 7d | 112.3505 | 0.2668 | 0.3265 | 2.0206 | 0.0389 | 0.0002 | 0.0070 | 0.0001 | 0.0922 | 0.0005 | 0.0014 | 0.0012 |
| Ref-NH 14d | 111.4816 | 0.3040 | 0.2984 | 2.1557 | 0.0420 | 0.0001 | 0.0077 | 0.0001 | 0.1169 | 0.0001 | 0.0015 | 0.0013 |
| Ref-NH 28d | 53.7944 | 0.2689 | 0.2891 | 2.0361 | 0.0363 | 0.0001 | 0.0060 | 0.0001 | 0.1090 | 0.0001 | 0.0014 | 0.0011 |

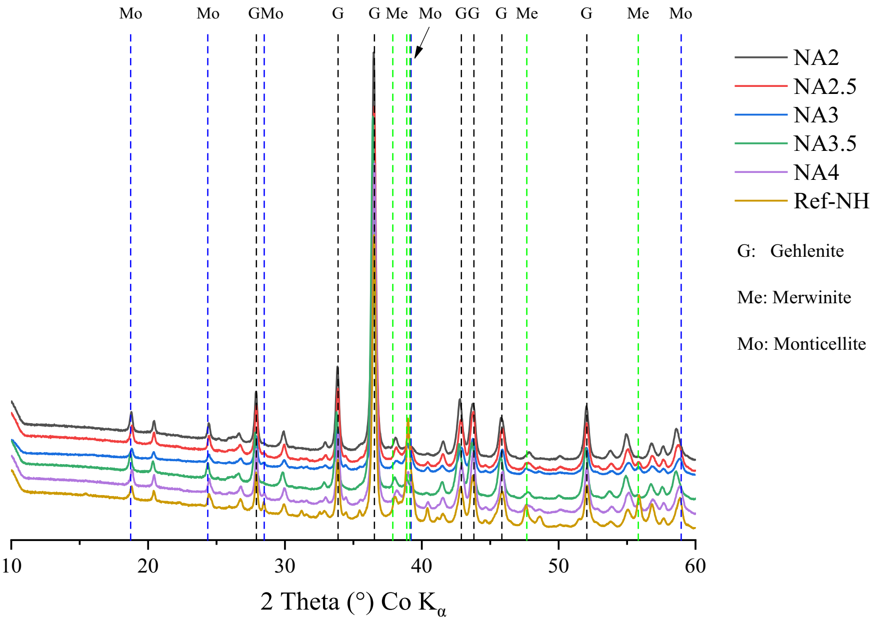

**Fig. A1.** XRD patterns of the SAAS pastes at 28 days after 1-h 900 °C heating.

**Table A7**
5 min leaching test of GGBS under different pH values of alkali leaching solution (mmol/L)

| pH | Si | Al | Mg |
|---|---|---|---|
| 13.5 | 2.2771 | 1.1721 | 0.0001 |
| 13 | 0.0831 | 0.0004 | 0.0002 |
| 12.5 | 0.2410 | 0.0383 | 0.0002 |
| 12 | 0.4122 | 0.0335 | 0.0001 |

## References

[1] A. Wang, Y. Zheng, Z. Zhang, K. Liu, Y. Li, L. Shi, D. Sun, The durability of alkali-activated materials in comparison with ordinary Portland cements and concretes: a review, Engineering 6 (2020) 695–706, https://doi.org/10.1016/j.eng.2019.08.019.

[2] J. Zhang, C. Shi, Z. Zhang, Z. Ou, Durability of alkali-activated materials in aggressive environments: a review on recent studies, Constr. Build. Mater. 152 (2017) 598–613, https://doi.org/10.1016/j.conbuildmat.2017.07.027.

[3] J. Osio-Norgaard, J.P. Gevaudan, W.V. Srubar, A review of chloride transport in alkali-activated cement paste, mortar, and concrete, Constr. Build. Mater. 186 (2018) 191–206, https://doi.org/10.1016/j.conbuildmat.2018.07.119.

[4] E. Adesanya, P. Perumal, T. Luukkonen, J. Yliniemi, K. Ohenoja, P. Kinnunen, M. Illikainen, Opportunities to improve sustainability of alkali-activated materials: a review of side-stream based activators, J. Clean. Prod. 286 (2021), https://doi.org/10.1016/j.jclepro.2020.125558.

[5] P. Chen, B. Ma, H. Tan, X. Liu, T. Zhang, C. Li, Q. Yang, Z. Luo, Utilization of barium slag to improve chloride-binding ability of cement-based material, J. Clean. Prod. 283 (2021), https://doi.org/10.1016/j.jclepro.2020.124612.

[6] T. Yang, Z. Zhang, F. Zhang, Y. Gao, Q. Wu, Chloride and heavy metal binding capacities of hydrotalcite-like phases formed in greener one-part sodium carbonate-activated slag cements, J. Clean. Prod. 253 (2020), https://doi.org/10.1016/j.jclepro.2020.120047.

[7] X. Ke, S.A. Bernal, O.H. Hussein, J.L. Provis, Chloride binding and mobility in sodium carbonate-activated slag pastes and mortars, Mater. Struct. Constr. 50 (2017), https://doi.org/10.1617/s11527-017-1121-8.

[8] Z. Yang, H. Fischer, R. Polder, Laboratory investigation of the influence of two types of modified hydrotalcites on chloride ingress into cement mortar, Cem. Concr. Compos. 58 (2015) 105–113, https://doi.org/10.1016/j.cemconcomp.2014.12.016.

[9] T. Liu, Y. Chen, Q. Yu, J. Fan, H.J.H. Brouwers, Effect of MgO, mg-Al-NO3 LDH and calcined LDH-CO3 on chloride resistance of alkali activated fly ash and slag blends, Constr. Build. Mater. 250 (2020), https://doi.org/10.1016/j.conbuildmat.2020.118865.

[10] Z.Y. Qu, Q.L. Yu, H.J.H. Brouwers, Relationship between the particle size and dosage of LDHs and concrete resistance against chloride ingress, Cem. Concr. Res. 105 (2018) 81–90, https://doi.org/10.1016/j.cemconres.2018.01.005.

[11] H. Ye, Autogenous formation and smart behaviors of nitrite- and nitrate-intercalated layered double hydroxides (LDHs) in Portland cement-metakaolin-dolomite blends, Cem. Concr. Res. 139 (2021), https://doi.org/10.1016/j.cemconres.2020.106267.

[12] J. Xu, Y. Song, Y. Zhao, L. Jiang, Y. Mei, P. Chen, Chloride removal and corrosion inhibitions of nitrate, nitrite-intercalated Mg–Al layered double hydroxides on steel in saturated calcium hydroxide solution, Appl. Clay Sci. 163 (2018) 129–136, https://doi.org/10.1016/j.clay.2018.07.023.

[13] X. Ke, S.A. Bernal, J.L. Provis, Uptake of chloride and carbonate by Mg-Al and Ca-Al layered double hydroxides in simulated pore solutions of alkali-activated slag cement, Cem. Concr. Res. 100 (2017) 1–13, https://doi.org/10.1016/j.cemconres.2017.05.015.

[14] S. Mundra, D.P. Prentice, S.A. Bernal, J.L. Provis, Modelling chloride transport in alkali-activated slags, Cem. Concr. Res. 130 (2020), 106011, https://doi.org/10.1016/j.cemconres.2020.106011.

[15] Y. Chen, Z. Shui, W. Chen, G. Chen, Chloride binding of synthetic Ca-Al-NO3 LDHs in hardened cement paste, Constr. Build. Mater. 93 (2015) 1051–1058, https://doi.org/10.1016/j.conbuildmat.2015.05.047.

[16] C. Forano, U. Costantino, V. Prévot, C.T. Gueho, Layered double hydroxides (LDH), Dev. Clay Sci. 5 (2013) 745–782, https://doi.org/10.1016/B978-0-08-098258-8.00025-0.

[17] S. Mallakpour, M. Dinari, Intercalation of amino acid containing chiral dicarboxylic acid between Mg-Al layered double hydroxide: preparation and characterization, J. Therm. Anal. Calorim. 119 (2015) 1123–1130, https://doi.org/10.1007/s10973-014-4166-8.

[18] A.A. Ramezanianpour, V.M. Malhotra, Effect of curing on the compressive strength, resistance to chloride-ion penetration and porosity of concretes incorporating slag, fly ash or silica fume, Cem. Concr. Compos. 17 (1995) 125–133, https://doi.org/10.1016/0958-9465(95)00005-W.

[19] R. Cao, S. Zhang, N. Banthia, Y. Zhang, Z. Zhang, Interpreting the early-age reaction process of alkali-activated slag by using combined embedded ultrasonic measurement, thermal analysis, XRD, FTIR and SEM, Compos. Part B Eng. 186 (2020), 107840, https://doi.org/10.1016/j.compositesb.2020.107840.

[20] D. Ravikumar, N. Neithalath, Electrically induced chloride ion transport in alkali activated slag concretes and the influence of microstructure, Cem. Concr. Res. 47 (2013) 31–42, https://doi.org/10.1016/j.cemconres.2013.01.007.

[21] J.L. Provis, S.A. Bernal, Geopolymers and related alkali-activated materials, Annu. Rev. Mater. Res. 44 (2014) 299–327.

[22] Q. Wan, F. Rao, S. Song, R.E. García, R.M. Estrella, C.L. Patiño, Y. Zhang, Geopolymerization reaction, microstructure and simulation of metakaolin-based geopolymers at extended Si/Al ratios, Cem. Concr. Compos. 79 (2017) 45–52, https://doi.org/10.1016/j.cemconcomp.2017.01.014.

[23] H.Zhe Jiao, S.Fei Wang, A.Xiang Wu, H.Ming Shen, J.Dong Wang, Cementitious property of NaAlO2-activated Ge slag as cement supplement, Int. J. Miner. Metall. Mater. 26 (2019) 1594–1603, https://doi.org/10.1007/s12613-019-1901-y.

[24] EN 196-1, in: En 196-1, 2005, pp. 1–33.

[25] G. Plusquellec, M.R. Geiker, J. Lindgård, J. Duchesne, B. Fournier, K. De Weerdt, Determination of the pH and the free alkali metal content in the pore solution of concrete: review and experimental comparison, Cem. Concr. Res. 96 (2017) 13–26, https://doi.org/10.1016/j.cemconres.2017.03.002.

[26] K. De Weerdt, G. Plusquellec, A. Belda Revert, M.R. Geiker, B. Lothenbach, Effect of carbonation on the pore solution of mortar, Cem. Concr. Res. 118 (2019) 38–56, https://doi.org/10.1016/j.cemconres.2019.02.004.

[27] B. Lina, L. Barbara, F.M. Alejandro, L. Christophe, Portlandite solubility and Ca2+ activity in presence of gluconate and hexitols, Cem. Concr. Res. 149 (2021), https://doi.org/10.1016/j.cemconres.2021.106563.

[28] C. Siakati, A.P. Douvalis, V. Hallet, A. Peys, Y. Pontikes, Influence of CaO/FeO ratio on the formation mechanism and properties of alkali-activated Fe-rich slags, Cem. Concr. Res. 146 (2021), https://doi.org/10.1016/j.cemconres.2021.106466.

[29] Influence of pozzolans and slag on the microstructure of partially carbonated cement paste by means of water vapour and nitrogen sorption experiments and BET calculations, Cem. Concr. Res. 40 (2010) 1723–1733, https://doi.org/10.1016/j.cemconres.2010.08.014.

[30] Z. Jia, R. Cao, C. Chen, Y. Zhang, Using in-situ observation to understand the leaching behavior of Portland cement and alkali-activated slag pastes, Compos. Part B Eng. 177 (2019), https://doi.org/10.1016/j.compositesb.2019.107366.

[31] N.T. Dung, T.J.N. Hooper, C. Unluer, Accelerating the reaction kinetics and improving the performance of Na2CO3-activated GGBS mixes, Cem. Concr. Res. 126 (2019), https://doi.org/10.1016/j.cemconres.2019.105927.

[32] X. Ke, S.A. Bernal, J.L. Provis, Controlling the reaction kinetics of sodium carbonate-activated slag cements using calcined layered double hydroxides, Cem. Concr. Res. 81 (2016) 24–37, https://doi.org/10.1016/j.cemconres.2015.11.012.

[33] A. Fernández-Jiménez, F. Puertas, Setting of alkali-activated slag cement. Influence of activator nature, Adv. Cem. Res. 13 (2001) 115–121, https://doi.org/10.1680/adcr.2001.13.3.115.

[34] S.R. Paudel, M. Yang, Z. Gao, PH level of pore solution in alkali-activated Fly-ash geopolymer concrete and its effect on ASR of aggregates with different silicate contents, J. Mater. Civ. Eng. 32 (2020) 04020257, https://doi.org/10.1061/(ASCE)MT.1943-5533.0003344.

[35] Yibing Zuo, Marija Nedeljković, Guang Ye, Pore solution composition of alkali-activated slag/fly ash pastes, Cem. Concr. Res. 41 (2019) 1257–1278, https://doi.org/10.1016/j.cemconres.2018.10.010.

[36] P. Li, J. Tang, Y. Bai, X. Chen, J. Chen, Experimental study on the pH for activating ground granulated blast-furnace slag activity at different temperatures, Sadhana - Acad. Proc. Eng. Sci. 44 (2019), https://doi.org/10.1007/s12046-019-1204-z.

[37] Y. Zuo, G. Ye, Lattice boltzmann simulation of the dissolution of slag in alkaline solution using real-shape particles, Cem. Concr. Res. 140 (2021), https://doi.org/10.1016/j.cemconres.2020.106313.

[38] A. Hajimohammadi, J.L. Provis, J.S.J. Van Deventer, Effect of alumina release rate on the mechanism of geopolymer gel formation, Chem. Mater. 22 (2010) 5199–5208, https://doi.org/10.1021/cm101151n.

[39] M. Bagheri, B. Lothenbach, M. Shakoorioskooie, K. Scrivener, Effect of different ions on dissolution rates of silica and feldspars at high pH, Cem. Concr. Res. 152 (2021), 106644, https://doi.org/10.1016/j.cemconres.2021.106644.

[40] Q. Li, H. Ma, Y. Tang, W. Chen, Combined effect of NaAlO2 and NaOH on the early age hydration of Portland cement with a high concentration of borate solution, Cem. Concr. Res. 144 (2021), https://doi.org/10.1016/j.cemconres.2021.106430.

[41] C.W. Hargis, A.P. Kirchheim, P.J.M. Monteiro, E.M. Gartner, Early age hydration of calcium sulfoaluminate (synthetic ye'elimite, C 4A3S¯) in the presence of gypsum and varying amounts of calcium hydroxide, Cem. Concr. Res. 48 (2013) 105–115, https://doi.org/10.1016/j.cemconres.2013.03.001.

[42] Effect of MgO, Mg-Al-NO3 LDH and calcined LDH-CO3 on chloride resistance of alkali activated fly ash and slag blends, Constr. Build. Mater. (2020), https://doi.org/10.1016/j.conbuildmat.2020.118865.

[43] I.G. Richardson, Tobermorite/jennite- and tobermorite/calcium hydroxide-based models for the structure of C-S-H: applicability to hardened pastes of tricalcium silicate, β-dicalcium silicate, Portland cement, and blends of Portland cement with blast-furnace slag, metakaol, Cem. Concr. Res. 34 (2004) 1733–1777, https://doi.org/10.1016/j.cemconres.2004.05.034.

[44] J.L. Provis, S.A. Bernal, Geopolymers and related alkali-activated materials, Annu. Rev. Mater. Res. 44 (2014) 299–327, https://doi.org/10.1146/annurev-matsci-070813-113515.

[45] M. Król, P. Rożek, D. Chlebda, W. Mozgawa, ATR/FT-IR studies of zeolite formation during alkali-activation of metakaolin, Solid State Sci. 94 (2019) 114–119, https://doi.org/10.1016/j.solidstatesciences.2019.06.004.

[46] G. Liu, M.V.A. Florea, H.J.H. Brouwers, The role of recycled waste glass incorporation on the carbonation behaviour of sodium carbonate activated slag mortar, J. Clean. Prod. 292 (2021), https://doi.org/10.1016/j.jclepro.2021.126050.

[47] E.R. McCaslin, C.E. White, A parametric study of accelerated carbonation in alkali-activated slag, Cem. Concr. Res. 145 (2021), https://doi.org/10.1016/j.cemconres.2021.106454.

[48] L. Fernández-Carrasco, J. Rius, C. Miravitlles, Supercritical carbonation of calcium aluminate cement, Cem. Concr. Res. 38 (2008) 1033–1037, https://doi.org/10.1016/j.cemconres.2008.02.013.

[49] R. Xiao, Y. Zhang, X. Jiang, P. Polaczyk, Y. Ma, B. Huang, Alkali-activated slag supplemented with waste glass powder: laboratory characterization, thermodynamic modelling and sustainability analysis, J. Clean. Prod. 286 (2021), https://doi.org/10.1016/j.jclepro.2020.125554.

[50] I. Perná, M. Šupová, T. Hanzlíček, Gehlenite and anorthite formation from fluid fly ash, J. Mol. Struct. 1157 (2018) 476–481, https://doi.org/10.1016/j.molstruc.2017.12.084.

[51] A.M. Rashad, G.M.F. Essa, Effect of ceramic waste powder on alkali-activated slag pastes cured in hot weather after exposure to elevated temperature, Cem. Concr. Compos. 111 (2020), https://doi.org/10.1016/j.cemconcomp.2020.103617.

[52] Z. Yan, Z. Sun, J. Yang, H. Yang, Y. Ji, K. Hu, Mechanical performance and reaction mechanism of copper slag activated with sodium silicate or sodium hydroxide, Constr. Build. Mater. 266 (2021), https://doi.org/10.1016/j.conbuildmat.2020.120900.

[53] F.B. Reig, J.V.G. Adelantado, M.C.M. Moya Moreno, FTIR quantitative analysis of calcium carbonate (calcite) and silica (quartz) mixtures using the constant ratio method. Application to geological samples, Talanta 58 (2002) 811–821, https://doi.org/10.1016/S0039-9140(02)00372-7.

[54] M. Criado, A. Fernández-Jiménez, A. Palomo, Alkali activation of fly ash: effect of the SiO2/Na2O ratio part I: FTIR study, Microporous Mesoporous Mater. 106 (2007) 180–191.

[55] U. Costantino, F. Leroux, M. Nocchetti, C. Mousty, Chapter 6 - LDH in physical, chemical, biochemical, and life sciences</sb:title>, Dev. Clay Sci. 5 (2013) 765–791, https://doi.org/10.1016/B978-0-08-098259-5.00026-3.

## Further Reading

[56] E. Bernard, W. Jan, B. Lothenbach, M. Urs, Stability of hydrotalcite (mg-Al layered double hydroxide) in presence of different anions, Cem. Concr. Res. 152 (2022), https://doi.org/10.1016/j.cemconres.2021.106674.